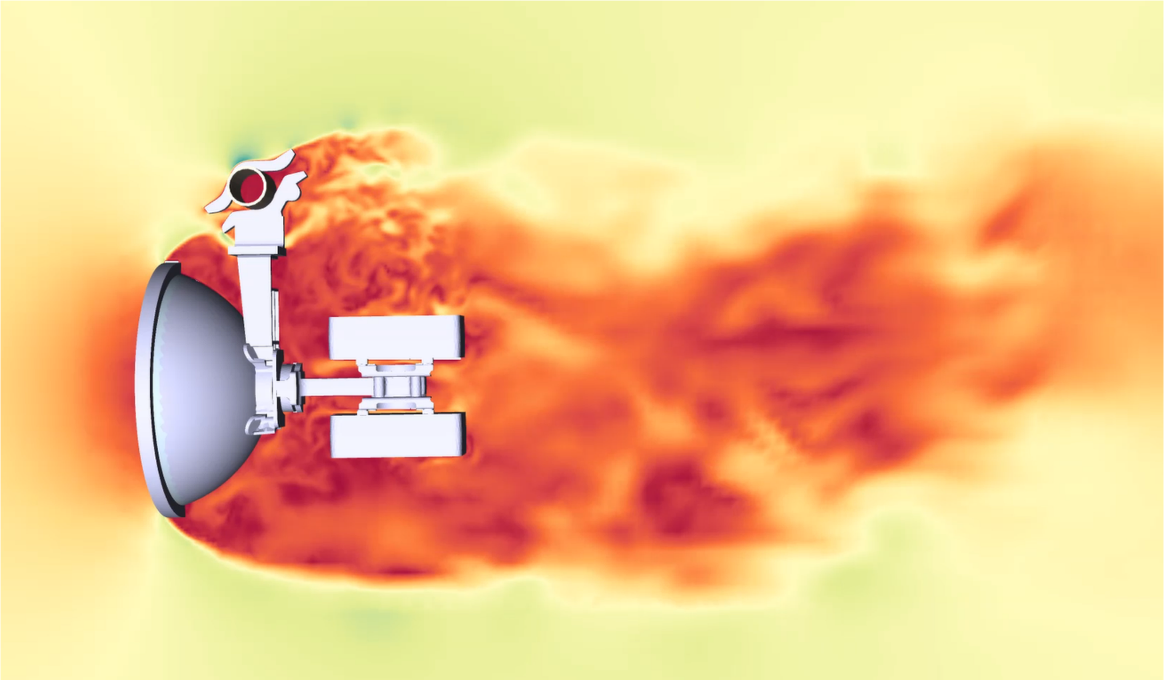

Process for analysis of wind-induced vibrations of antennas

A two-way Fluid-Structure Interaction simulation in Ansys Workbench, validated with wind tunnel testing

Master's thesis in Applied Mechanics

Maria Hörnell
Erica Lundberg

DEPARTMENT OF MECHANICS AND MARITIME SCIENCES

CHALMERS UNIVERSITY OF TECHNOLOGY
Gothenburg, Sweden 2022
www.chalmers.se

Master's thesis 2022

Process for analysis of wind-induced vibrations of antennas

A two-way Fluid-Structure Interaction simulation in Ansys Workbench, validated with wind tunnel testing

Maria Hörnell
Erica Lundberg

Department of Mechanics and Maritime Sciences
Division of Fluid Dynamics
Chalmers University of Technology
Gothenburg, Sweden 2022

Process for analysis of wind-induced vibrations of antennas
A two-way Fluid-Structure Interaction simulation in Ansys Workbench,
validated with wind tunnel testing
MARIA HÖRNELL, ERICA LUNDBERG

Supervisor: Peter Melin and Fredrik Öhrby, Ericsson AB
Examiner: Lars Davidson, Department of Mechanics and Maritime Sciences

Master's Thesis 2022:41
Department of Mechanics and Maritime Sciences
Division of Fluid Dynamics
Chalmers University of Technology
SE-412 96 Gothenburg
Telephone +46 31 772 1000

Cover: Antenna subjected to a constant wind load showing the deformation and the turbulent flow around the structure. Additional plots of the velocity field can be found in Appendix A.5.

Typeset in LaTeX
Printed by Chalmers Reproservice
Gothenburg, Sweden 2022

Process for analysis of wind-induced vibrations of antennas
A two-way Fluid-Structure Interaction simulation in
Ansys Workbench, validated with wind tunnel testing
Master's thesis in Applied Mechanics
MARIA HÖRNELL, ERICA LUNDBERG
Department of Mechanics and Maritime Sciences
Division of Fluid Dynamics
Chalmers University of Technology

Abstract

Deflection and vibrations of antennas that are a part of a transmission line result in a significant drop in performance. This is due to the performance being highly dependent on whether the antenna lobe hits the target. A small deflection of the antenna structure caused by wind load results in a great deflection of the antenna lobe.

In this project, a simulation process is developed to predict the wind-induced vibrations of Ericsson's antenna structures. The process uses a two-way Fluid-Structure Interaction setup, which couples a structural and a fluid solver. To validate the simulation process, wind tunnel testing at Chalmers University of Technology was conducted. The testing included cases of constant wind load, different angles of incoming wind and hammer impulse tests. A damping ratio of 2.78% was calculated from the experimental data using the method of logarithmic decrement. A method for creating a fluid domain was developed to resolve the turbulent flow around the antenna using the criteria set by the LES model.

The simulation results were compared to the experimental data and correlated well in frequency. Certain patterns of the deflection of the antenna from the experimental testing were well captured by the simulation process.

The computational time of the simulation process was optimised by increasing the time step size. The larger time step size resulted in a decrease of almost one-third of the computational time of a finer time step size without losing considerable accuracy. The decreased computational time is favourable when using this process in the industry.

Keywords: two-way Fluid-Structure Interaction (FSI), antenna, vibrations, wind load, simulation, process, performance, wind tunnel, experiment,

Acknowledgements

We would like to express a special thank you to our excellent supervisors at Ericsson, Peter Melin and Fredrik Öhrby, who supported us through this whole project. Even though this was new territory for all four of us, their help was very valuable to have throughout the process. Also, thank you to Paul Hutcheson and Tobias Berg from Ansys, for sharing their expertise and advice during the whole simulation setup. We would have been stuck so many more times if it wasn't for them. Thank you to Valery Chernoray, who assisted us during the wind tunnel experiments, and Lars Davidsson, our examiner at Chalmers.

To anyone else we encountered along the way who in some way helped us with this project, thank you for all the knowledge you shared with us.

Nomenclature

Abbreviations

BOI	Body Of Influence
CAD	Computer-Aided Design
CFD	Computational Fluid Dynamics
CFL	Courant-Friedrichs-Lewy
DNS	Direct Numerical Simulation
FFT	Fast Fourier Transform
FSI	Fluid-Structure Interaction
LES	Large Eddy Simulation
PCC	Phantom Camera Control
RANS	Reynolds-averaged Navier-Stokes
SBES	Stress-Blended Eddy Simulation
TKE	Turbulent Kinetic Energy

Greek letters

Δ	Cell width
Δx	Cell length
δ	Logarithmic decrement
ϵ	Turbulent dissipation rate
ζ	Damping ratio
θ	Phase angle
μ	Dynamic viscosity
μ_{sgs}	Turbulent viscosity of the sub-grid scale

ρ	Density
$\boldsymbol{\sigma}^R$	Reynolds stress tensor
τ_w	Wall shear stress
ϕ	Amplitude
$\{\boldsymbol{\phi}\}$	Mode shape
ω	Angular frequency

Roman upper case letters

A_{max}	Maximum amplitude
$\boldsymbol{\{}C\}$	Damping matrix
C_f	Skin friction coefficient
C_s	Smagorinsky’s coefficient
$\boldsymbol{\{}K\}$	Stiffness matrix
$\boldsymbol{\{}M\}$	Mass matrix
Q	Amplification factor
T	Time period
U	Free stream velocity, velocity
U_τ	Friction velocity

Roman lower case letters

f	Frequency
$\boldsymbol{f}(t)$	Time-dependent load vector
$\boldsymbol{g}$	Gravity vector
k	Turbulent kinetic energy
k_{res}	Resolved turbulent kinetic energy
k_{sgs}	Sub-grid scale turbulent kinetic energy
l_0	Integral length scale
l_{sgs}	Sub-grid length scale
n	Positive integer for number of successive amplitude peaks
p	Pressure
$\bar{p}$	Averaged pressure vector
t	Time

$\boldsymbol{u}$	Displacement vector, Velocity vector
$\dot{\boldsymbol{u}}$	Velocity vector
$\ddot{\boldsymbol{u}}$	Acceleration vector
$\bar{\boldsymbol{u}}$	Averaged velocity vector
$u(t)$	Peak amplitude at time t
y^+	Non-dimensional wall thickness
y_p	Wall distance

Table of Contents

1

Introduction

Mobile networks are used all over the world and are the cornerstone of the networked society, where everything shall be connected. Antennas are an important part of this network and many of Ericsson's applications.

For microwave systems, the antenna is a part of creating a transmission line where two antennas are directed towards each other. The performance of this transmission is highly dependent on whether the antenna lobe hits the other antenna. At higher transmission frequencies, the lobe becomes more narrow and the wind-induced vibration of the antennas may create a significant drop in performance. Therefore, it is of great interest to find a way to predict how the antennas move during wind load in order to develop a solution.

1.1 Background

In the industry today, the most common way to predict the effect of wind load on antenna structures is by using Eurocodes. The EN Eurocodes are the European standards for structural design and EN 1991-1-4, in particular, can be used to predict wind actions onto structures [1]. This standard used for predicting wind loads is not a simulation process. Instead, the Eurocode guides how to determine the effects of wind loads using characteristic values of mean wind, terrain, neighbouring structures and other parameters involved. The characteristic values are determined from basic values of wind velocity or the velocity pressure [2].

Another common way to determine the effects of wind load is to calculate the pressure from a *Computational Fluid Dynamics* (CFD) solver. The pressure is applied as a static load in a mechanical solver and a structural analysis can be conducted. This method is not time-dependent and does not factor in any dynamic loads or fluctuations that occur naturally when a structure is subjected to wind load.

Neither of the previously mentioned methods, the EN 1991-1-4 or the static analysis, captures the effects of the changing motion of a real wind load. Instead, they provide a guideline or an estimate of the wind effects. This guideline is useful for a quick assessment but will not provide any details about the dynamic effects.

The antennas operating today transmit signals at frequencies as high as 80 GHz and the higher the frequency, the more sensitive the antennas are to vibrations and deflections. For example, an antenna with an 80 GHz transmission frequency has a very narrow beamwidth of 0.8°. Imagine this antenna

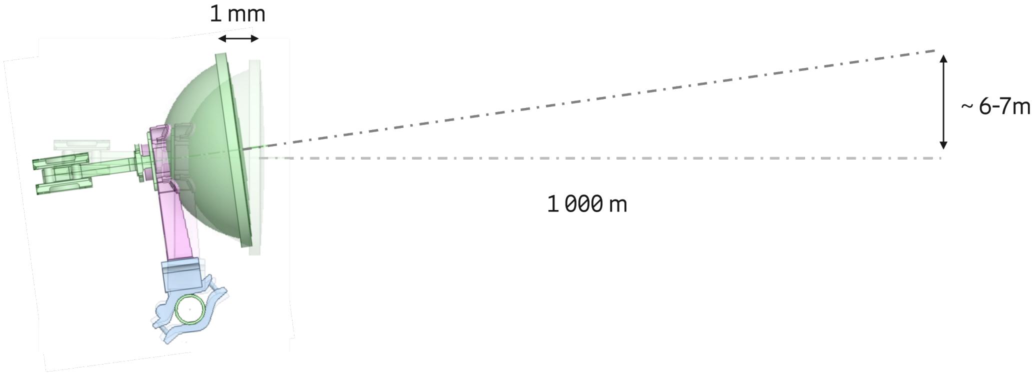

Figure 1.1: An example of how a deflection of 1 mm of the transmitting antenna results in an antenna lobe deflection of approximately 6–7 m.

facing another antenna 1 km away. If the antenna deflects 1 mm, the antenna lobe will deflect 6–7 m, see Figure 1.1. If the antenna were to deflect 1 mm in the opposite direction, the antenna lobe would deflect 6–7 m in the opposite direction as well. These small deflections can occur due to vibrations and swaying that are not captured by the Eurocode standard or the static analysis.

As technology evolves with even higher frequencies, the problem with wind-induced vibrations will continue to grow. Therefore, it is of great interest to accurately capture and understand the behaviour of the deformation that is caused by the wind in order to find solutions to the problem. This work aims at creating a process for conducting these types of wind load simulations using a two-way *Fluid-Structure Interaction* (FSI), further explained in Section 2.1.

1.2 Objectives

The main objectives of this Master's thesis are to:

- Develop a simulation process to predict wind-induced vibrations of antennas
- Produce a process guide in the form of a collection of documents with guidance to Ericsson

These main objectives involve the following sub-goals:

- Conduct experiments to gain data for validation of the displacement and frequency of the structure
- Evaluate the damping ratio
- Create simulation domains for both structural and fluid solver
- Validate the simulation results against experimental data

1.3 Limitations

In reality, the wind is a chaotic and turbulent phenomenon which makes it difficult to model. In this project, the wind is limited to coming from a fixed direction with a constant velocity in the wind tunnel. It was not a possibility to conduct the same experiment with an oscillating wind load due to limitations of the wind tunnel.

The most prominent limitation of this project was the time. Both in the sense of the time span of this project and computational ability. The computational ability was affected by computational time and the number of available cores. The server used for the simulation had 24 cores available for use.

As stated in Section 1.2, one of the main objectives is to develop a simulation process to predict the wind-induced vibrations of a general antenna system. In this project, only one full-scale antenna model is used for both the experiment and the simulations, specifically a round antenna system with a diameter of 0.3 m. The mounting of the antenna is also limited to one specific pole, used for both the experiment and simulations. In reality, the antenna can be mounted on different kinds of poles and masts that will have an impact on the movement of the antenna structure.

1.4 Software

This Master's thesis work uses the Ansys Workbench 2021R2 platform and its solvers for the simulation process. The Fluent modules are used for creating the mesh and solving the fluid flow and the Mechanical solver is used for solving the structural deformation. The Mechanical solver consists of modules such as static structural, transient structural and modal, all used in this project. In the simulation process, the Mechanical solver and the Fluent solver are connected by the System Coupling module that handles the simulation data transfer. The results are post-processed in the visualization tool Ansys EnSight. For the data processing from the wind tunnel testing, Matlab and Microsoft Excel are used for calculations and plotting.

1.5 Structure and coordinate system

In this project, parts of the structure and directions will occasionally be mentioned. The antenna used in the simulations and in the experiment is shaped similarly to a half sphere with a diameter of 0.3 m. To help navigate through the names and terms for the geometry and coordinate systems used in this report, the necessary information has been compiled in this section.

The numbering and description of the parts of the antenna structure can be found in Table 1.1. The numbers correspond to the parts shown in Figure 1.2. The coordinate system can also be observed in Figure 1.2. The x-direction is in line with a horizontal back-and-forth motion, the y-direction represents a horizontal sideways motion and the z-direction is the vertical, up-and-down motion of the antenna.

Table 1.1: Numbering and description of the parts mentioned in this report.

Number in Figure 1.2	**Name**	**Description**
1	Radome	Refers to the circular front plate of the antenna
2	Attachment	Refers to the component connecting the antenna to the pole
3	Pole	The pole that represents a mast fixture and holds the antenna
4	Radios	Radio components attached on the backside of the antenna

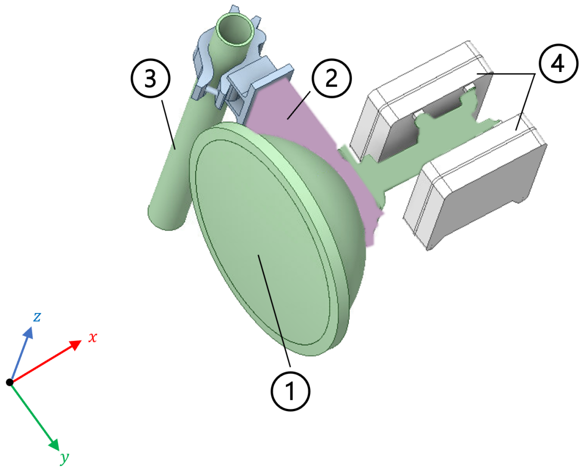

Figure 1.2: A schematic of the parts mentioned in this report with a view from above. 1) Radome, 2) attachment, 3) pole and 4) radios.

2

Theory

The methods and results presented in this project are based on several fundamental models and concepts which are presented in this chapter. The chapter starts with the concept of an FSI simulation, continues with the modal analysis and damping ratios necessary for the structural part of this thesis and finally explains the necessary turbulence models and parameters for the fluid simulation.

2.1 Fluid-Structure Interaction

In nature, everything that happens has a counter effect. The treetops bend by the wind and the oceans clash and break against the mountainside. Nature interacts between elements and objects, which is fundamental to consider when simulating the effects of wind on a structure, i.e., a Fluid-Structure Interaction (FSI) simulation.

A fluid-structure interaction describes the type of problem where interaction between the mechanical part and the fluid part has a mutual dependency. The mechanical structure and properties affect the motion of the flow and the fluid forces acting on the structure causes deformation and deflection of the structure [3]. Solving an FSI case is crucial for many engineering problems, e.g., effects on the fluid flow, structural parameters, material selection, fatigue, etc [4]. However, these kinds of problems are often complex to solve analytically and therefore have to be solved either experimentally or numerically. In this project, both experimental and numerical solutions will be analysed.

The FSI problem can be divided into two main categories; the one-way FSI and the two-way FSI. For the one-way FSI, only the fluid pressure is transferred to the mechanical part that deforms. The solution is static from which a time-independent structural analysis can be conducted. This procedure does not factor in how the structural deformation affects the flow.

For this Master's thesis work, the numerical solution will be performed with a two-way FSI, where the fluid forces and the deformation of the structure interact in a coupled simulation. The coupled simulation is time-dependent and transfer data between the fluid domain and structural domain at each time step, creating a continuous interaction.

2.2 Modal analysis

It is of great interest to perform a modal analysis to find the eigenfrequencies and eigenmodes of the structure before starting the two-way FSI simulation. These frequencies and modes can be used when deciding the time step size of the simulations and validating that the displacements and vibrations are captured. It is also important to be aware of natural frequencies at which the structure will resonate and cause destructive vibrations [5]. The modal analysis shows the dynamic characteristics of the structure and depicts properties such as damping and stiffness which needs to be factored in to accurately set up the simulation [6].

In this project, the Modal module in Ansys Workbench is used to perform the modal analysis, but it is important to understand the underlying theory behind the computation.

Modal analysis is a linear dynamics analysis that uses the equation of motion to find the frequencies and mode shapes of the structure and is written as:

$$[\boldsymbol{M}]\{\ddot{\boldsymbol{u}}\} + [\boldsymbol{C}]\{\dot{\boldsymbol{u}}\} + [\boldsymbol{K}]\{\boldsymbol{u}\} = \{\boldsymbol{f}(t)\} \tag{2.1}$$

where M is the mass matrix, C is the damping matrix, K is the stiffness matrix and $f(t)$ is the time-dependent load vector. $\ddot{u}$, $\dot{u}$ and u denote the acceleration vector, the velocity vector and the displacement vector respectively.

This equation is simplified for the modal analysis since the eigenfrequencies and eigenmodes are independent of loads. Furthermore, the effects of damping are rather complex and often have to be determined through experimental testing. Therefore, the effects are left out of the governing equation and are added as a parameter in the calculation. The governing equation for the free and undamped system for the modal analysis can be observed in equation (2.2) [7].

$$[\boldsymbol{M}]\{\ddot{\boldsymbol{u}}\} + [\boldsymbol{K}]\{\boldsymbol{u}\} = \{\boldsymbol{0}\} \tag{2.2}$$

Solving equation (2.2) for the displacement means solving an eigenvalue problem. The solution takes the form of a harmonic motion and is written as:

$$\{\boldsymbol{u}\} = \{\boldsymbol{\phi}\}_i \sin(\omega_i t + \theta_i) \tag{2.3}$$

where ϕ denotes the amplitude, ω is the angular frequency and θ is the phase angle. Index i describes every point on the structure.

By deriving the expression in equation (2.3) twice with respect to time, the governing equation in equation (2.2) can be rewritten as:

$$\begin{gathered} ([\boldsymbol{K}] - \omega_i^2[\boldsymbol{M}])\{\boldsymbol{\phi}\} = \{0\} \\ |[\boldsymbol{K}] - \omega^2[\boldsymbol{M}]| = 0 \end{gathered} \tag{2.4}$$

where it is utilised that to have a non-zero solution, the matrix $([\boldsymbol{K}] - \omega_i^2[\boldsymbol{M}])$ has to be singular, i.e., the determinant has to be equal to zero. Solving equation (2.4) gives ω which is the angular frequency of the structure, whereas $\{\boldsymbol{\phi}\}$ represents the mode shape [6]. The angular frequency of the structure is related to the natural frequency according to equation (2.5).

$$f_i = \frac{\omega_i}{2\pi} \tag{2.5}$$

2.3 Damping ratio

The damping ratio is an efficiency measurement of a structure's ability to remove energy through radiation or dissipation during cyclic or near-cyclic conditions [8]. The effects of damping are important to consider when analysing vibrations and are rather complex. Mathematically, it is convenient to view the damping as proportional to the velocity of the structure. However, in doing so, the physical model would have to be viscous which is not a characteristic observed in real structures. Instead, a friction model is used for structures, which in turn is problematic mathematically [9].

There are different forms of mechanical damping. This project mainly considers the internal, structural damping which includes frictional losses, dissipation due to relative movement in the fluid, and damping caused by the material of the structure [10].

In order to calculate the damping ratio, two methods are used, namely the method of logarithmic decrement and the half-power bandwidth method. Both methods use experimental input data from a hammer impulse test, further explained in Section 3.2.

2.3.1 Method of logarithmic decrement

The method of logarithmic decrement uses a time-domain approach where the natural logarithm of the amplitude ratio between two peaks is measured, see Figure 2.1.

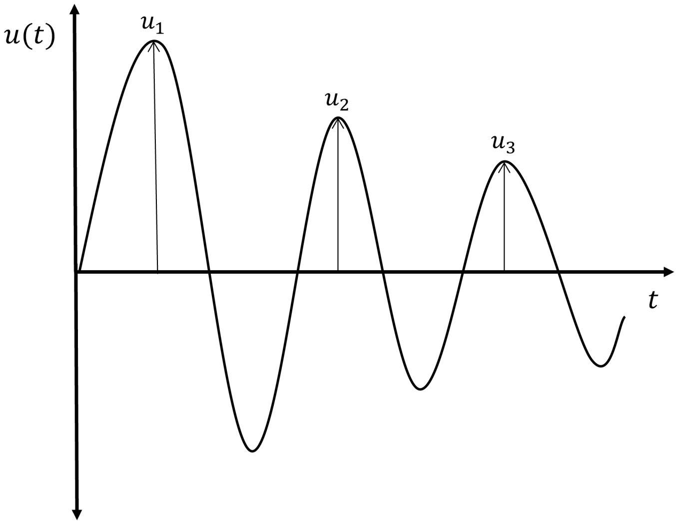

Figure 2.1: Example of a displacement plot over time. The positive amplitude peaks are needed for the calculation of the logarithmic decrement which can be calculated by inserting the amplitude of the peaks into equation (2.6)*.*

The logarithmic decrement, δ, is then calculated using the following equation:

$$\delta = \frac{1}{n} \ln \frac{u(t)}{u(t+nT)} \tag{2.6}$$

where $u(t)$ is the peak amplitude at time t, $u(t+nT)$ is the peak amplitude at n periods away. The variable n has to be a positive integer corresponding to successive amplitude peaks [11].

These peaks in this project is the amplitude of the vibrations of the structure at a fixed point. The damping ratio can in turn be obtained from the logarithmic decrement using the following formula:

$$\zeta = \frac{1}{\sqrt{1 + \left(\frac{2\pi}{\delta}\right)^2}} \tag{2.7}$$

where ζ is the sought damping ratio [11].

2.3.2 Half-power bandwidth method

The half-power bandwidth method uses *Fast Fourier Transform* (FFT) to convert the data obtained from experimental testing from the time domain into the frequency domain. The oscillating data used in the previous logarithmic decrement method is instead transformed to amplitude peaks at discrete frequencies. The half-power bandwidth method estimates the damping ratio from the amplification factor, Q. Q is the ratio between the natural frequency and the width between half-power points and is calculated from the following equation:

$$Q = \frac{f_n}{\Delta f} = \frac{f_n}{f_2 - f_1} \tag{2.8}$$

where f_1 and f_2 are the half-power points corresponding to the amplitude $A_{max}/\sqrt{2}$, see Figure 2.2.

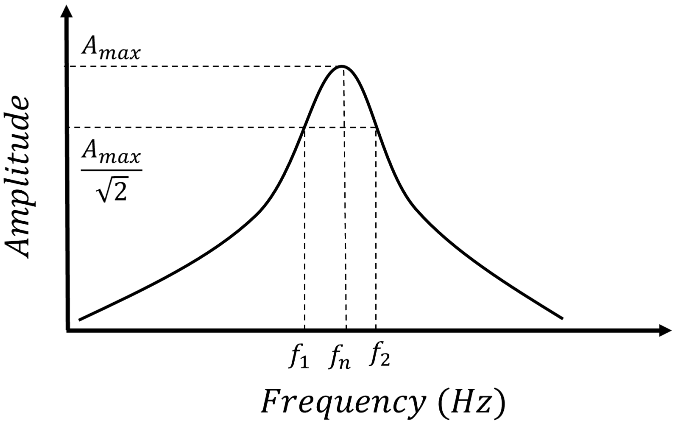

Figure 2.2: The important points of the half-power bandwidth method. A_{max} is the peak value from the FFT graph corresponding to the natural frequency, f_n. f_1 and f_2 are the half-power points corresponding to the amplitude $A_{max}/\sqrt{2}$.

The damping ratio can then be calculated using equation (2.9) [12].

$$\zeta = \frac{1}{2Q} \tag{2.9}$$

2.4 Turbulence

Turbulence is a natural phenomenon that is present all around us; in the wind, oceans and even in our bloodstream. Turbulence is usually described as an irregular, disorganized behaviour of the flow, unlike the steady, ordered laminar flow which acts smoothly in intact parallel layers. Turbulence, in its disorganisation, breaks these layers and creates new formations in the form of eddies and vortices. These eddies appear in a range of different sizes, where the larger scales carry more energy than the small scales.

The *Turbulent Kinetic Energy*, TKE, can be represented by a curve that is based on empirical studies, shown in Figure 2.3. The x-axis shows the wavenumber, which is an inverse of the eddy diameter, d, defined as $wavenumber = \frac{2\pi}{d}$ [13]. So in the figure, low wavenumbers indicate large eddies and large wavenumbers give smaller eddies. The total TKE of the flow is the area below the curve of the figure. Different types of turbulence models will solve this area with different approaches. The most intricate method of them will solve every eddy in the whole flow, from large to small.

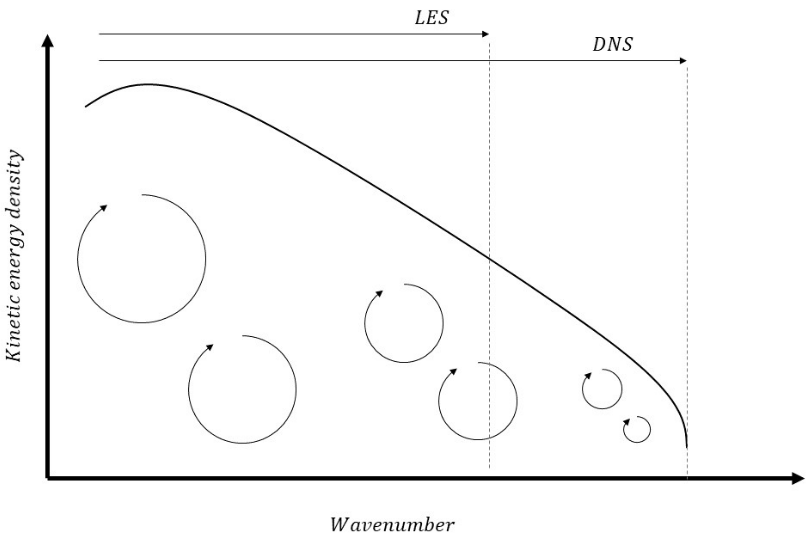

Figure 2.3: The energy spectrum. Kinetic energy density versus wavenumber creates an area under the curve which represents the total turbulent kinetic energy.

When computing a fluid flow we need turbulence models to capture the behaviour. There are different types of models to compute a flow, which are more or less modelled. The foundation of solving any fluid flow are the governing Navier-Stokes equations. The incompressible Navier-Stokes equations in convective form is presented in equation (2.10) [14].

$$\rho(\frac{\partial \boldsymbol{u}}{\partial t} + \boldsymbol{u} \cdot \boldsymbol{\nabla} \boldsymbol{u}) = -\boldsymbol{\nabla} p + \mu \nabla^2 \boldsymbol{u} + \rho \boldsymbol{g} \tag{2.10}$$

In equation (2.10), ρ is the density of the fluid, $\boldsymbol{u}$ is the velocity vector, t is the time, $\boldsymbol{\nabla} p$ is the pressure gradient, μ is the dynamic viscosity of the fluid and $\boldsymbol{g}$ is the gravity vector.

2.4.1 Turbulence models

The Navier-Stokes equations can be solved completely numerically. This approach is called a *Direct Numerical Simulation* (DNS) where all parts of the turbulent flow are resolved, from smallest to largest of scales, with no modelling assumptions. This approach is very demanding and computationally heavy, therefore not commonly used by engineers. In the industry, instead, approaches with modelling and filtering are preferred. Models and filters will ease the computational load. Two main approaches used are the *Reynolds-averaged Navier-Stokes* (RANS) and *Large Eddy Simulation* (LES).

RANS

RANS is a time-averaged version of Navier-Stokes, shown below. The whole range of turbulent scales is modelled with the RANS-based modelling approach and is time-independent, which makes it less computationally demanding.

$$\rho(\bar{\boldsymbol{u}} \cdot \boldsymbol{\nabla}\bar{\boldsymbol{u}}) = -\boldsymbol{\nabla}\bar{p} + \mu\nabla^2\bar{\boldsymbol{u}} + \boldsymbol{\nabla} \cdot \boldsymbol{\sigma}^R + \rho\boldsymbol{g} \tag{2.11}$$

The averaging creates an additional term where $\boldsymbol{\sigma}^R$ is the Reynolds stress tensor which accounts for the turbulent fluctuations in the flow.

LES

In an LES computation, the large eddies are computed while the small eddies are modelled. You could say it filters away the small, sub-grid scales which are modelled to ease the computational load. The larger scales of eddies are explicitly computed, which means that the governing equations are solved numerically. This approach is heavier than RANS with respect to computational load.

Hybrid model

In the industry, it is important to save time and resources where possible. Therefore hybrid models, combining RANS and LES, are common. The hybrid model used in the software, see Section 1.4, is the *Stress-Blended Eddy Simulation* (SBES) model. This model applies RANS solutions in near-wall regions and in ambient regions that are not exposed to heavy turbulence. In the turbulent areas, LES is applied. By using LES only where necessary, computational time and load are kept as low as possible without time-averaging the large turbulent eddies.

2.4.2 Mesh

It is of great importance when running an LES simulation to ensure that the cell sizes of the mesh are small enough to capture the turbulent behaviour of the flow and all of its vortices. Therefore, an essential part of setting up the simulation domain is creating a suitable mesh. The mesh is restricted by the LES demands since they are stricter than the demands of a RANS mesh.

The mesh is evaluated by estimating how much of the TKE, k, is resolved. Calculated as the ratio:

$$ratio = \frac{k_{res}}{k} = \frac{k_{res}}{k_{res} + k_{sgs}} \tag{2.12}$$

where k_{res} is the resolved TKE and k_{sgs} is the sub-grid scale TKE. These two together make up the total TKE, as $k = k_{res} + k_{sgs}$. For a sufficient LES mesh the resolved TKE should be above 80% [13], where the smallest scales are modeled. Figure 2.4 shows an illustration of what it would look like in the previously presented TKE plot.

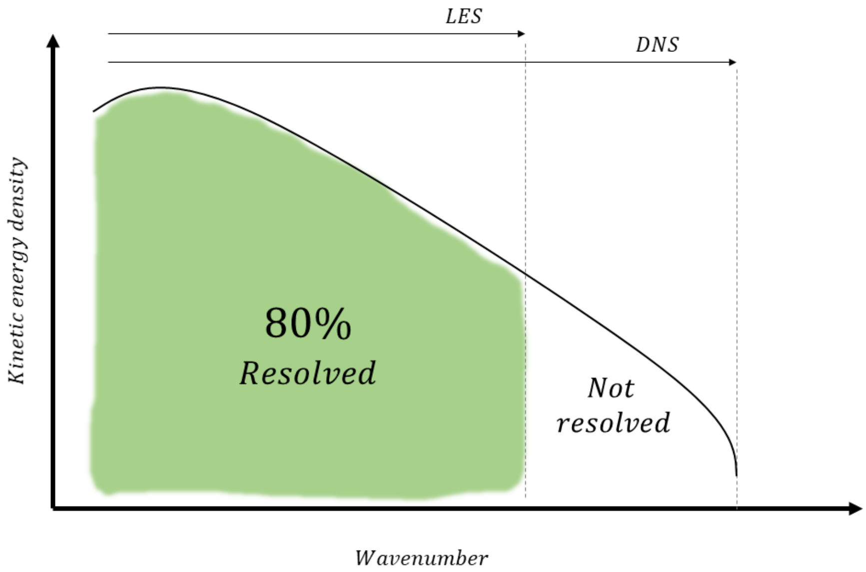

Figure 2.4: Illustration of modeled and resolved turbulence. The not resolved area is modeled turbulence.

The resolved TKE is calculated by summing the mean square of the fluctuating velocities, in all three directions [13], and is written as:

$$k_{res} = \frac{1}{2}\left(\overline{(u')^2} + \overline{(v')^2} + \overline{(w')^2}\right) \tag{2.13}$$

where u', v' and w' are the fluctuating velocities in the x, y and z-direction. The sub-grid scale TKE, k_{sgs}, is collecting the TKE smaller than the mesh grid size. Part of attaining this is defining the sub-grid length scale, l_{sgs}. This is a length scale that represents the size of the eddies that are too small to be resolved. The sub-grid scale TKE is defined as:

$$k_{sgs} = \left(\frac{\mu_{sgs}}{\rho l_{sgs}}\right)^2 \tag{2.14}$$

where μ_{sgs} is the turbulent viscosity of the sub-grid scale and ρ is density of the fluid.

The sub-grid length scale can then be expressed as:

$$l_{sgs} = C_S \cdot \Delta \tag{2.15}$$

where the Smagorinsky's coefficient, C_S, is commonly approximated to 0.1. The coefficient always need to fulfill $C_S < 1$ to provide a length smaller than the grid. Δ is the cell width.

2.4.3 Integral length scale

The mesh will be evaluated from the integral length scale, l_0, derived from turbulence-dependent variables. Since the flow is built up by different sizes of eddies mixed together, one area will not have one specific length on the eddies. To be able to evaluate the flow more easily an approximation of all these different sizes need to be made. This is done with the integral length scale, which represents an averaged eddy size based on the turbulent kinetic energy of several eddies, see Figure 2.5. It is calculated as:

$$l_0 = \frac{k^{3/2}}{\epsilon} \tag{2.16}$$

where ϵ is the turbulent dissipation rate.

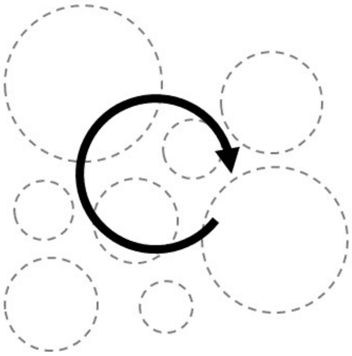

Figure 2.5: Visualisation of how different sizes of eddies are averaged to one integral length scale.

It is recommended that 80% of the eddies are resolved for a proper LES. One common estimation to achieve 80% resolution is that the width of the mesh-cell should be one-fifth of the integral length scale [13]. This means that the energy averaged eddy can be fitted in a 5x5 mesh, see Figure 2.6. The cell width, Δ, is approximated as:

$$\Delta = \frac{l_0}{5} \tag{2.17}$$

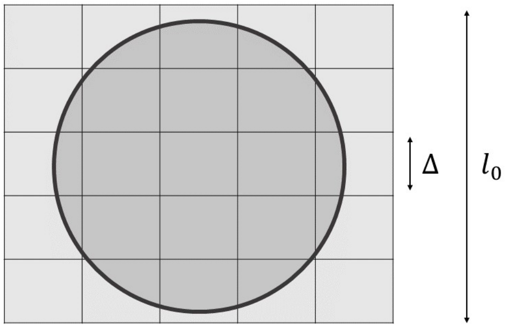

Figure 2.6: Illustration of an eddy fitted in a 5x5 mesh.

2.5 Simulation parameters

For the simulations to be constructed correctly, several parameters are important to consider. These parameters are either input of the setup or output of the simulation. The most essential parameters will be presented in the following chapters, giving a theoretical foundation for the method and results in Chapter 4.

2.5.1 $\mathbf{y^+}$ value

When it comes to simulating a turbulent flow, it is important to be aware of the effects that the presence of walls has on the fluid flow. The frictional effects from the no-slip condition at the walls create a mean flow shear in the boundary layer. The boundary layer can be divided into three sub-regions, namely, the viscous sub-layer, the transition region called the buffer layer, and the log-region [15]. The y^+ value is a non-dimensional wall thickness parameter used to describe the grid height of the cell closest to the wall. The formula for the y^+ value can be written as:

$$y^+ = \frac{\rho U_\tau y_p}{\mu} \tag{2.18}$$

where ρ is the density of the fluid, μ is the dynamic viscosity and y_p is the wall distance. The other terms related to the y^+ value are the friction velocity, U_τ, and the wall shear stress, τ_w, which has the following equations:

$$U_\tau = \sqrt{\frac{\tau_w}{\rho}} \tag{2.19}$$

$$\tau_w = \frac{1}{2} C_f \rho U^2 \tag{2.20}$$

where U is the free stream velocity and C_f is the skin friction coefficient [16].

The desired value of y$^+$ is case dependent, but as a general rule, it should be $y^+ \leq 5$ or between $30 \leq y^+ \leq 300$ for RANS-based turbulence models to avoid the buffer layer. The buffer layer is to be avoided due to the fact that it can not be represented correctly by any wall model, unlike the other two layers.

2.5.2 Time step size

Choosing the right time step size for the simulation is crucial for a complete resolution of the FSI simulation. The FSI needs an even smaller time step size than the standard, purely fluid or purely mechanical simulation, due to its complexity of combining the solid and fluid regions. The time step size can be chosen with several different methods.

One method is based on the structure's eigenfrequency and is a recommended approach by Ansys expertise [17]. The time step size is chosen based on a couple of inputs. First, an estimation can be made by splitting the time period of the eigenfrequency of the structure into smaller pieces, which is dependent on the geometry and the materials of the structure. The time step size strongly correlates with the *Courant-Friedrichs-Lewy* (CFL) number. The CFL number, amongst other factors, is used to validate that both mesh and time step is sized correctly. How the CFL number is chosen is described more thoroughly in Section 2.5.3.

The eigenfrequency used is the first modal frequency that is obtained from the modal analysis described in Section 2.2. The time period is obtained by inverting this frequency according to:

$$T = \frac{1}{f} \tag{2.21}$$

where T is the time period and f is the frequency. The time period needs to have sufficient resolution, i.e., sufficient amount of time steps within this time period. Figure 2.7 visualises how half a time period is divided into time steps. When simulating a stand-alone fluid flow, 20–50 time steps per period can be sufficient if the case is less complex. Due to the added complexity of the FSI, 70–100 steps per time period are needed for full resolution [17]. When optimising the process, one wants to ensure there are a sufficient amount of steps, yet not exaggerated. That would cause an excessively long computational time, which is undesirable.

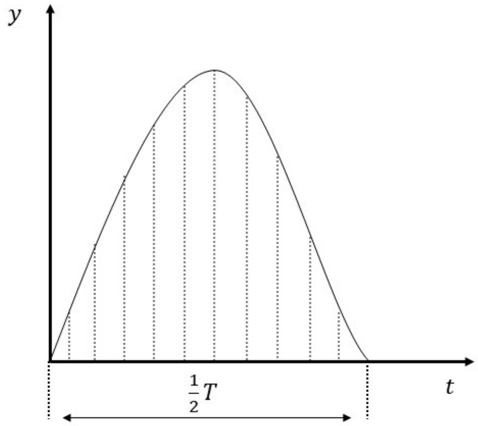

Figure 2.7: Visualisation of how the time period is divided into time steps. In the figure, half a time period is shown. The y-axis represents an arbitrary variable, e.g., displacement.

2.5.3 CFL-number

The Courant-Friedrichs-Lewy (CFL) number is a form of stability criterion and is used in the process of choosing the size of the time step. The CFL number is dependent on the cell size, Δx, the time step size, Δt, and the velocity, U, of the fluid flow [18].

$$CFL = \frac{U\Delta t}{\Delta x} \tag{2.22}$$

For a numerical solution to be accurate, the CFL number needs to be set to the constraint $CFL \leq 1$. Simplified, this implies that the fluid flow will travel less than the width of a cell in the time step given. This is illustrated in Figure 2.8. If the CFL number is larger than 1, the fluid has moved over more than one whole cell within the time step, creating a jump between calculated cells. This can be quite intuitive if the equation (2.22) and Figure 2.8 are combined. To ensure an accurate numerical solution, all cells should be calculated and therefore the constraint of $CFL \leq 1$ is desirable.

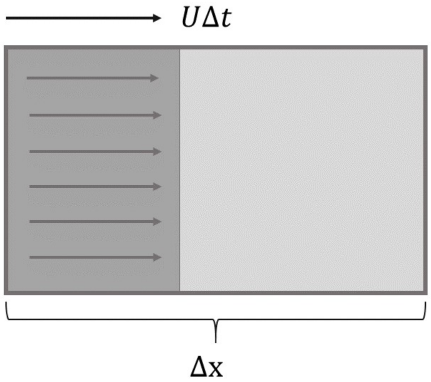

Figure 2.8: Example of a fluid's transportation within a cell in one time step for a CFL-number below 1. $U\Delta t$ is the fluid's movement within the cell and Δx is the cell width.

3

Wind tunnel testing

A reliable way to validate any research is through experiments. In this project, both a wind tunnel test and a hammer impulse test were conducted. The wind tunnel test will give a sense of the movement of the structure under constant wind load, while the hammer impulse test generates data to calculate the damping and eigenfrequency of the structure. The movement will further be compared to the simulation results, to verify that they move in a similar manner. The damping and eigenfrequency from the experiment will lay the foundation for the structural setup of the simulation. The test setup will be presented and followed by an explanation of the different test cases and ending with the calculation procedure of the damping ratio of the antenna structure.

3.1 Wind tunnel set-up

The wind tunnel test was performed in the Large-Scale Low Turbulence Subsonic Wind Tunnel at Chalmers University of Technology. The wind tunnel is a semi-closed loop tunnel that can operate at wind speeds up to 60 m/s [19]. The wind tunnel has a test section area of 1.28×1.25 m^2 and a test section length of 3 m [20].

The antenna with attachment, support, and radios was provided by Ericsson. To ensure that the antenna was securely attached, it was bolted to a mounting device located under the test section. An accelerometer was attached to the top of the radome of the antenna, see Figure 3.1. At the same position, a sticker with a dotted grid was mounted to assist a high-speed camera. The opening in the floor, visible in the figure, was closed before testing.

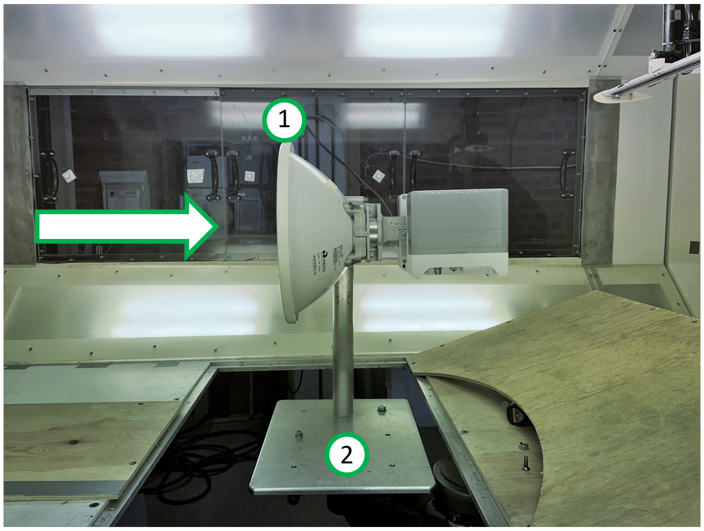

Figure 3.1: The setup of the wind tunnel testing. The arrow indicates the direction of the wind flow.
1) The position of the accelerometer and the measuring point for the high-speed camera.
2) The structure is bolted to the mounting device.

A 12-bit Phantom Miro M340 high-speed camera was used to capture the movement during the experiment with 3000 fps and a 768 × 768 resolution. The camera was mounted in the ceiling of the wind tunnel and captured the same location as the accelerometer. It used the dotted grid with a 1 mm distance between the points to accurately measure the displacement, see Figure 3.2.

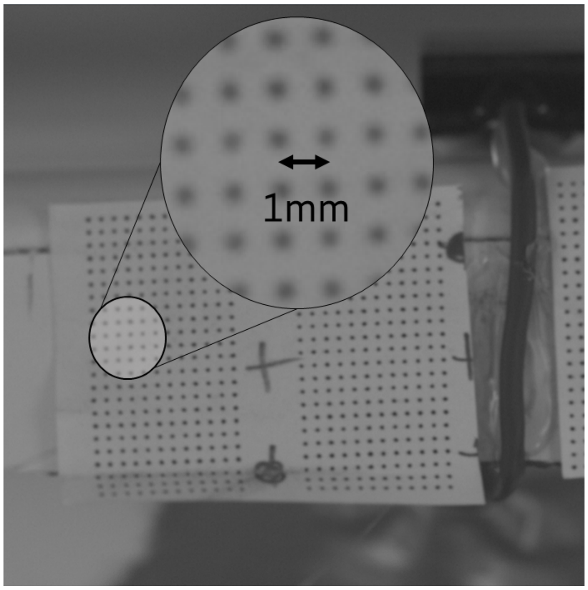

Figure 3.2: An image of the grid that was used to accurately measure the movement of the antenna subjected to wind load. The distance between the points is 1 mm.

Using the *Phantom Camera Control* (PCC) software, the time and displacements could be calculated from the captured raw files using an algorithm based on cross-correlation, which has an accuracy of 0.1 pixels [21].

3.2 Test procedure

Two velocities were measured during the tests, specifically 15 m/s and 40 m/s. 15 m/s corresponds to the average wind speed that antennas are subjected to. 40 m/s on the other hand is the maximum operational wind speed that this antenna model is built to handle. Note that maximum operational wind speed is not the same as maximum survival wind speed.

In combination with the velocities, two different angles were measured. First, the 0° angle, which is when the incoming wind hits the antenna from the front, is displayed in Figure 3.1. The other angle was 45°, which meant the antenna setup was rotated 45° clockwise on the supporting pole. The purpose of the two angles was to ensure that the worst case of wind load was selected for the antenna. Combining these velocities and angles resulted in four different cases.

In addition to the wind speed tests, three hammer impulse tests were conducted. The hammer impulse test was carried out by hitting the structure with a rubber hammer at a specific location and measuring the oscillating displacement of the measuring point caused by the impact. The three impact locations were on the back of the radio, along with the antenna attachment, and the top of the pole as is shown in Figure 3.3. Each test from the tunnel provided the displacement data of the measuring point on top of the antenna in two directions, the x-direction and the y-direction, see Figure 1.2. These directions corresponded to a back-and-forth motion and a sideways motion of the antenna.

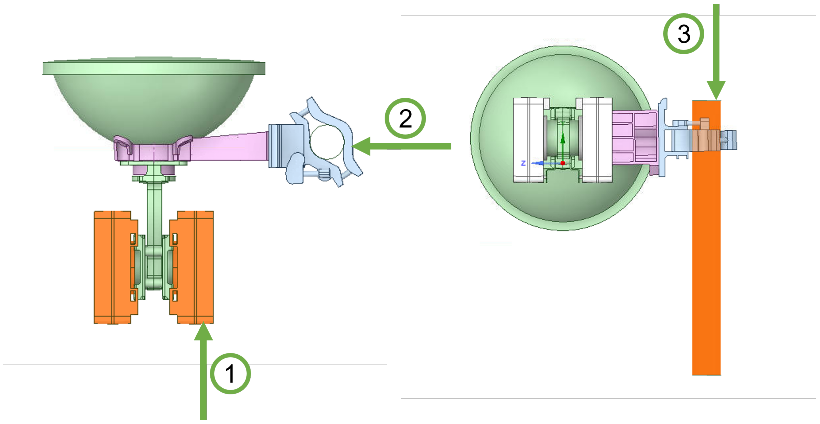

Figure 3.3: The three locations of impact for the hammer impulse test. 1) Backside radio, 2) antenna attachment and 3) top mast.

The accelerometer used was not sensitive enough to capture the movement and vibrations of the antenna. Therefore, the results presented in this project are from the high-speed camera only.

3.3 Results from the constant wind load tests

The results from the test cases with constant wind load, as described in Section 3.2, are presented below.

As previously mentioned, the two angles, 0° and 45°, were chosen because they could represent two possible worse case scenarios. An incoming wind hitting the radome of the antenna from the front is believed to have a large deflection since the area subjected to the wind load is large. The same can be said for a wind load with an incoming angle of 45° since the radios and the side of the antenna bowl would provide additional surfaces for the wind to catch on to.

During the wind tunnel experiments, it was important that the wind had reached a steady flow before the data was collected. This means that the displacement data from the experiment does not show any initial deformation or settling behaviour. Instead, what is observed in the results presented below, is the deformation caused by the turbulence, resulting in vibrations of the structure.

In Figure 3.4, the displacement in the x-direction for the wind load of 15 m/s can be observed. Figure 3.4a shows the case when the incoming wind load is striking the antenna straight from the front, at an incoming angle of 0°. The distance between the highest peak and the lowest peak is approximately 0.1 mm. For the case with an incoming angle of 45°, seen in Figure 3.4b, the distance between the highest peak and the lowest peak is approximately 0.062 mm.

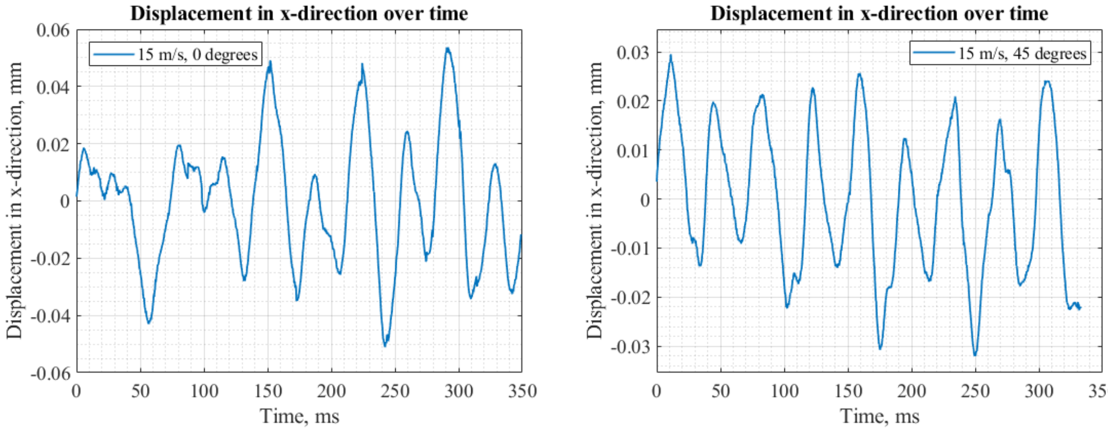

(a) 0° *(b) 45°*

Figure 3.4: Displacement of the antenna from the cases with a constant wind load of 15 m/s measured in the x-direction. The angle of the incoming wind is: (a) 0° and (b) 45°.

A similar comparison between the incoming wind load angle of 0° and 45° can be observed in Figure 3.5. For the case of 0°, the distance between the highest peak and the lowest peak is approximately 1.7 mm, whereas, for the case of 45°, the distance between the highest peak and the lowest peak is approximately 0.31 mm.

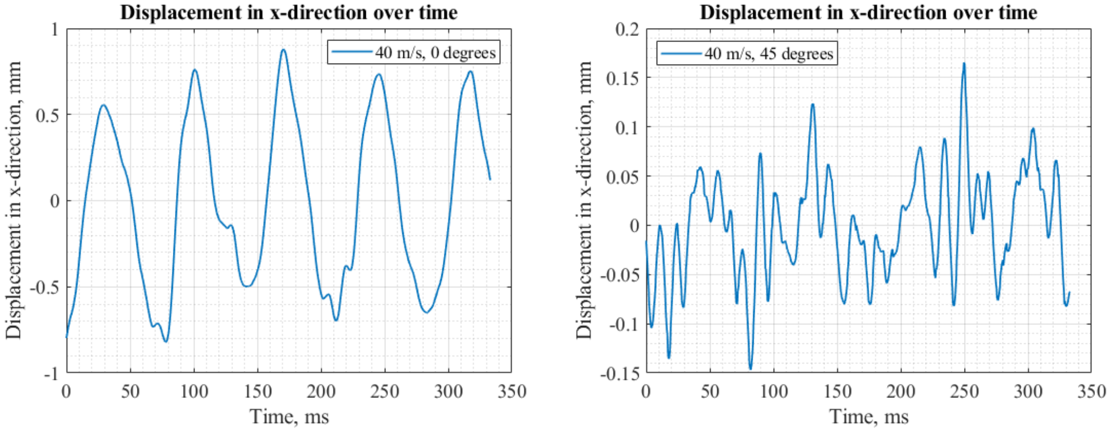

(a) 0° *(b) 45°*

Figure 3.5: Displacement of the antenna from the cases with a constant wind load of 40 m/s measured in the x-direction. The angle of the incoming wind is: (a) 0° and (b) 45°.

Comparing the results between the two angles of incoming wind, the deflection of the antenna in the x-direction is smaller for the cases with an incoming wind load angle of 45°, compared to the angle of 0°. For the 15 m/s cases, the range of displacement differs by approximately 0.04 mm between the two angles, shown in Figure 3.4. For the 40 m/s case the displacement differs by approximately 1.4 mm between the angles, see Figure 3.5. This shows that the cases where the antenna structure is rotated 45° are more aerodynamic and do not deflect as much compared to the 0° cases.

The comparison between results from the wind tunnel and the results from the simulations, presented in Chapter 5, will use results from the 0° angle and a wind load of 40 m/s. Because the displacement is greater, it will be easier to distinguish the movement of the antenna from possible noise and other disturbances. The displacement plots for the y-direction can be found in Appendix A.1.

3.4 Damping ratio and eigenfrequency from the tests

The damping ratio was calculated using the method of logarithmic decrement and the half-power bandwidth method described in Section 2.3. The calculations were made using the measured data from the hammer impulse test as well as from the test with constant wind load when possible.

As previously described in Section 3.2, the hammer impulse test was measured on top of the radome and had three different locations of impact; the backside of the radio, the antenna attachment and on top of the pole. The frequencies could be obtained from the built-in FFT algorithm in Matlab using the time and the displacement from the hammer impulse test as input. These three tests produced the same resonance frequency, which can be observed in Figure 3.6. From the displacement plot, seen in Figure 3.7, the frequency of the oscillations can be calculated by extracting the period of the curve. The oscillations have a frequency of approximately 12.3 Hz.

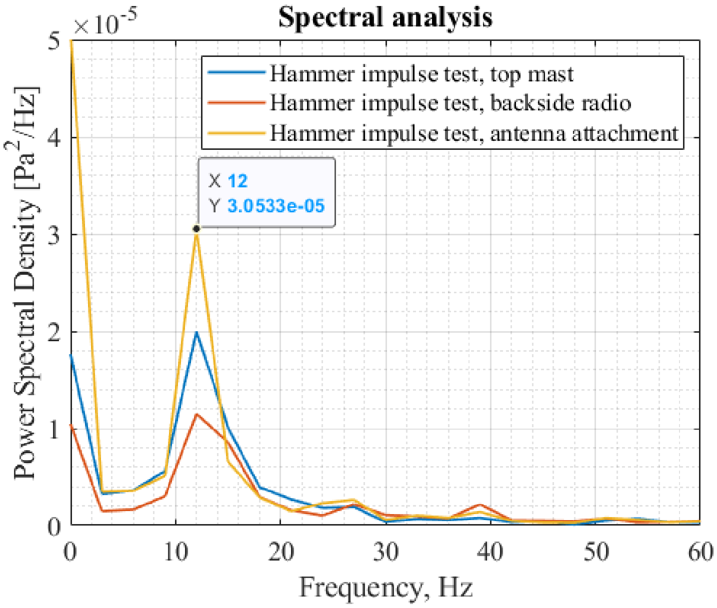

Figure 3.6: The graph shows the spectral analysis for the three hammer impulse tests. The resonance frequency is around 12 Hz.

The displacement response from the hammer impulse tests differed, mainly because the impact force and direction differed for the tests. The oscillating displacement over time from the hammer test with impact location at the backside of the antenna is presented in Figure 3.7. The data from the other two tests can be found in Appendix A.2. In hindsight, one thing to be noted is that the hammer impulse test from the top mast gave the most scattered results and is due to having an impact angle mostly from the z-direction (above) whereas the high-speed camera only captured deformation in x- and y-direction (in the plane). Therefore, one could argue that the results from the top mast test should be neglected.

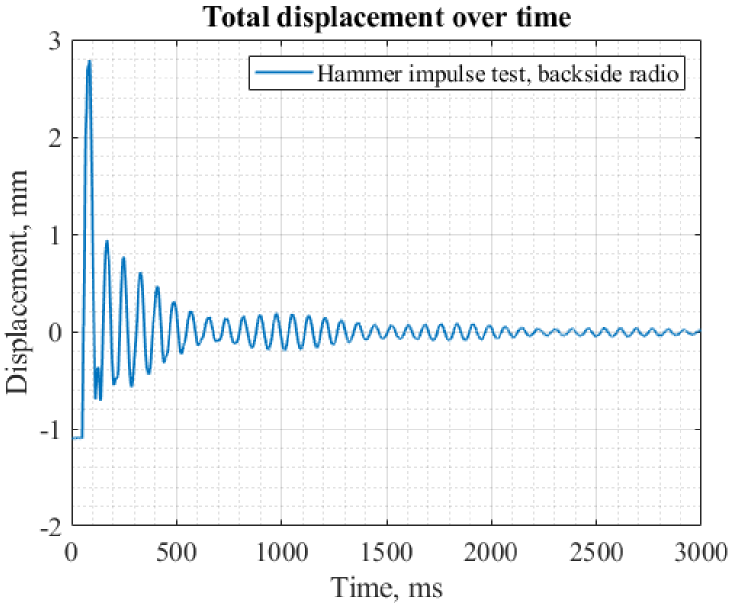

Figure 3.7: The graph shows the displacement of the measuring point on the antenna over time for the hammer impulse test. The location of impact is on the backside of the radio.

As can be observed in Figure 3.7, there seem to be two eigenmodes present in the oscillations. One mode is oscillating with a frequency of approximately 13 Hz and the other mode is oscillating with a frequency of approximately 1.25 Hz. This can be seen by the bump shapes in the curve caused by the two modes interacting, which results in increase and reduction in amplitude.

3.4.1 Damping ratio using the method of logarithmic decrement

From the data obtained from the wind tunnel testing, the peak amplitudes were extracted and used as input for the logarithmic decrement method in equation (2.6). The result was in turn used in equation (2.7) to calculate the damping ratio. The extraction of peak amplitudes and the calculations were made using Matlab.

From the displacement graph, there are two possible approaches for the method of logarithmic decrement. The first one is to consider all peaks and the second one is to only look at a local interval before the second eigenmode causes the amplitude to increase again, see Figure 3.8.

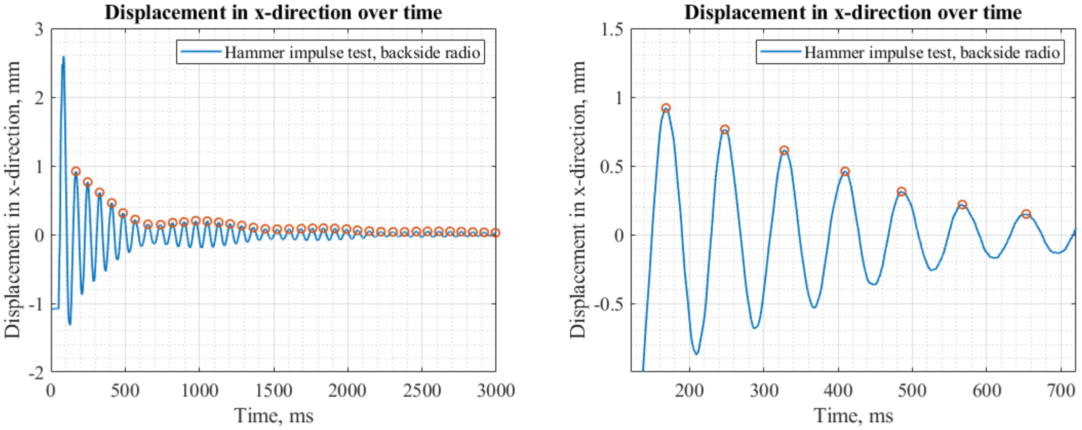

(a) Approach 1 *(b) Approach 2*

Figure 3.8: Illustration of the two approaches for calculating the damping ratio using the method of logarithmic decrement. (a) Approach 1: using all peaks (b) Approach 2: using a local interval of peaks.

The result of the calculation of the damping ratio for all of the three hammer impulse tests using Approach 1 and Approach 2 can be found in Table 3.1 and Table 3.2 respectively. A combined average of the damping ratio in each direction is presented in Table 3.3.

Table 3.1: The calculated damping ratios for the three tests in x, y and xy-direction using Approach 1. An average damping ratio in each direction is shown at the bottom of the table.

Approach 1	**Damping ratio in x-direction**	**Damping ratio in y-direction**	**Damping ratio in xy-direction**
Top mast	0.82%	0.54%	0.10%
Backside radio	1.30%	10.03%	5.71%
Antenna attachment	7.13%	10.88%	10.03%
Average	**3.08%**	**7.15%**	**5.28%**

Table 3.2: The calculated damping ratios for the three tests in x, y and xy direction using Approach 2. An average damping ratio in each direction is shown at the bottom of the table.

Approach 2	**Damping ratio in x-direction**	**Damping ratio in y-direction**	**Damping ratio in xy-direction**
Top mast	2.1%	1.54%	1.76%
Backside radio	4.58%	2.95%	5.21%
Antenna attachment	1.55%	2.98%	2.35%
Average	**2.74%**	**2.49%**	**3.11%**

Table 3.3: The averaged damping ratio for the structure obtained from combining the ratios in all three directions.

	Approach 1	**Approach 2**
Average damping ratio	5.17%	2.78%

Evaluating the results calculated using the method of logarithmic decrement, the first approach used all peaks including the peaks where a second mode could be distinguished. This second mode is believed to be interference from the mounting device. The damping ratios calculated using the first approach gave quite different results for each direction and the average ratio. The damping ratio should ideally be the same value no matter the direction, but considering the method of logarithmic decrement, the measuring direction should be in the same direction as the incoming force. Therefore, the results from the hammer impulse test for the backside radio are of particular interest for this method.

The second approach proved to be the better way to calculate the damping ratio. By focusing on a local interval with a steadily decrease in amplitude for each successive peak, the damping ratio was found to be quite consistent.

3.4.2 Damping ratio using the half-power bandwidth method

As opposed to the method of logarithmic decrement, the half-power bandwidth method can also be used on the experimental data where the antenna was subjected to a constant wind load, in addition to the hammer impulse tests.

For the half-power bandwidth method, an FFT algorithm computed the frequencies of the obtained data. As described in Section 2.3, the frequencies corresponding to the amplitude $A_{max}/\sqrt{2}$ were extracted and used in equation (2.8). The damping ratio could then be calculated using equation (2.9).

In Figure 3.9, the spectral analysis plot for the hammer impulse test on the antenna attachment is shown. The amplitude, $A_{max}/\sqrt{2}$, is displayed as a horizontal line and the frequencies corresponding to the intersection between the line and the curve are shown as well. These frequencies are needed for the half-power bandwidth method.

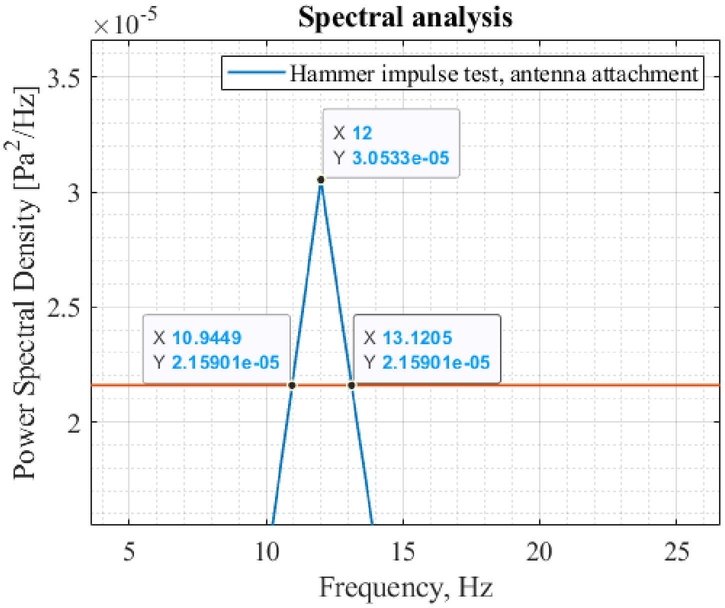

Figure 3.9: Spectral analysis of the hammer impulse test on the antenna attachment. The horizontal line corresponds to the $A_{max}/\sqrt{2}$ amplitude of $3.05E{-}5$ Pa^2/Hz which is used to determine the necessary frequencies for the half-power bandwidth method.

Using equation (2.8) and (2.9), the damping ratio could be calculated for all four wind load cases and the three hammer impulse tests. The results are presented in Table 3.4 and 3.5 and the associated graphs can be found in Appendix A.3.

Table 3.4: The damping ratio calculated from the constant wind load cases using the half-power bandwidth method.

Case	**15 m/s 0°**	**15 m/s 45°**	**40 m/s 0°**	**40 m/s 45°**
Damping ratio	22.38%	2.00%	8.84%	8.45%

Table 3.5: The damping ratio calculated from the hammer impulse tests using the half-power bandwidth method.

Case	**Top mast**	**Backside radio**	**Attachment**
Damping ratio	12.50%	18.47%	9.06%

As can be observed in Table 3.4 and Table 3.5, the half-power bandwidth method gave damping ratios over a wide range, from 2% to 22%. Even though this method is a well-known and used method, it was not ideal for this project. To be able to get accurate results using this method, a shaker modal testing with a sine sweep or random frequency vibration profiles would be better suited to get a smoother and more accurate spectral analysis curve.

4

FSI Simulation

The Fluid-Structure Interaction (FSI) simulation consists of two coupled solvers and one upstream fluid solver, which can be observed in the flowchart in Figure 4.8. This chapter is divided into a structural section, a fluid section and finally the combined FSI setup. In the structural section, the settings and setup of the mechanical model are presented. This includes parts such as material parameters, mesh elements and contact definitions. Results from the modal analysis and how the damping ratio study was conducted are also presented.

The fluid section presents how the meshing of the fluid domain was generated, including boundary layers and an investigation of crucial parameters. Finally, details of how the LES resolution was estimated and deemed acceptable, and how the time step size was chosen for the simulation are presented. The chapter ends with a section about the connected mechanical and fluid solvers in a two-way FSI and finally how the simulation could be optimised for industrial use.

4.1 Structure

The structural module is part of several aspects of this project such as the modal analysis, the damping ratio and the FSI analysis. Therefore, it is important to accurately portray the structural model of the antenna. In this section, details about the mechanical setup, the modal analysis and validation of the damping ratio are presented and discussed.

4.1.1 Preparation and setup of the structural solver

The structural model has to be run through a modal analysis and confirm that the damping ratio matches the experimental data by simulation. In order to accurately simulate the deformation of the structure, it is important that the model is a proper representation of the real structure. However, a too detailed model will result in a lengthy computational time, especially when it comes to the two-way FSI simulation. Removing small details such as bolts, rounded corners, and indents from the model will allow for a slightly coarser mesh which is beneficial for the computational time and with a diminutive effect on the deformation.

The deformation of the structure depends on several factors that need to be taken into account. Parameters that will affect the structural behaviour are mainly material parameters such as stiffness and density, the centre of gravity of the components and the meshing of the structure. It is therefore of great importance that these parameters are accurate to the real model.

The material parameters for the antenna were obtained by weighing each component and then dividing it by the volume of the *Computer-Aided Design* (CAD) model of the component, thus obtaining the density of the component. This allowed for changes in the CAD geometry while maintaining the weight of each component the same as for the real model. This is under the assumption that each component is homogeneous and that the centre of gravity is located where it would be for a homogeneous component. As for material parameters, e.g., stiffness and elasticity, the default material properties in Ansys Workbench corresponding to the materials in the real antenna were used.

In the Mechanical module, the choice between using solid elements, shell elements and solid shell elements was considered. In the final setup, solid shell elements were used for the pole and solid elements for the rest of the structure with a mesh size of 1E-2 m. The reasoning behind this is that shell elements better capture the bending that occurs for thinner geometries in relation to mesh size. However, for the mapping between the fluid solver and the mechanical solver to match, solid elements are preferred. Therefore, the solid shell elements are best suited for the pole in this case.

As for boundary conditions, the bottom of the pole was assigned to be fixed to represent the mounting in the wind tunnel. It is assumed that the plate bolted to the mounting device in the wind tunnel is infinitely stiff, therefore the plate is removed for the simulation to save computational time.

One factor that affects the results greatly is the contact definition between the components. During this process, a bonded contact area matching the physical bolts proved to be a good way to model the contacts, see Figure 4.1.

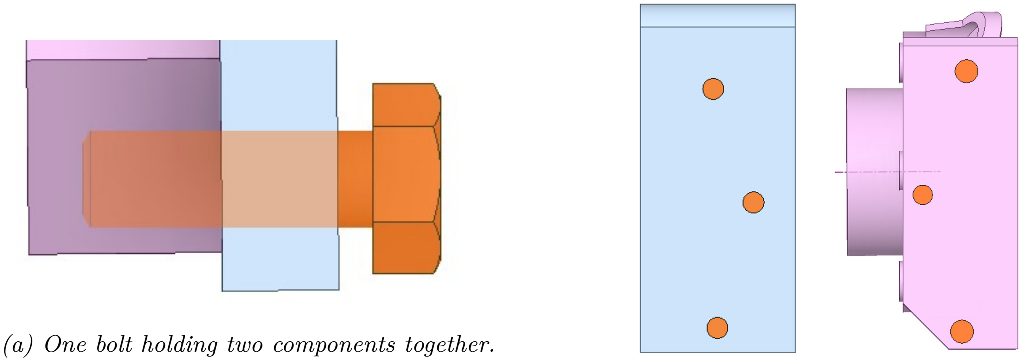

(a) One bolt holding two components together.

(b) The contact area of the two components.

Figure 4.1: The contact area has been defined to give an accurate representation of the physical bolts holding the components together. (a) A CAD representation of how a bolt is holding two components together. (b) The two components with contact areas are highlighted in orange. The dimensions of the circular contact areas match the physical bolts in size and location.

When the materials, element type and size, contacts and boundary conditions were set, the model was ready to use for the modal analysis, the damping study and the two-way FSI.

4.1.2 Modal analysis

Using the setup procedure described in Section 4.1.1, the modal analysis could be conducted. Using the material density for each component and using solid shell elements for the pole, the frequency for the first mode was 13.49 Hz. The eigenfrequencies corresponding to the six first eigenmodes can be found in Table 4.1.

Table 4.1: The eigenfrequencies corresponding to the first six eigenmodes of the structure.

Mode	**1**	**2**	**3**	**4**	**5**	**6**
Frequency [Hz]	13.49	18.421	32.84	38.08	61.672	66.7

Compared to the eigenfrequency of the first mode from the experimental testing, the frequency obtained from the simulation is higher by almost 1.2 Hz. This is reasonably due to differences in the simulation model compared to the physical model. The assumption of the components being homogeneous, the stiffness of the pole or other material properties is likely to differ due to a lack of certainty in the real model.

4.1.3 Validation and tuning of the damping ratio

To validate the calculated damping ratio, the hammer impulse test was replicated in a transient simulation. Since the hammer impact results in an instantaneous hit, it was found easier to replicate the simulation using the deformation caused by the hammer as an initial condition in the same location as the impact and letting the antenna go, which in this report is referred to as a *drag-and-drop test*.

Using a static calculation to obtain the force that corresponded to the initial displacement, a transient two-step calculation was executed to capture the damped oscillating movement of the antenna. The first step of the two-step calculation was to apply the initial force and the second step was to deactivate the force, meaning that it was let go from the initial displacement. By using the calculated damping ratio and eigenfrequency from the modal analysis as input for the structural damping controls, the resulting deflection of the antenna over time could be compared to the experimental results. The drag-and-drop test for different damping ratios was simulated and the comparison between these results and the result from the experiment is shown in Section 5.1.

4.2 Fluid

The fluid domain requires a proper setup to ensure correct results. It needs to capture the turbulent behaviour of the flow to mimic reality as closely as possible. This is attained by choosing a mesh size and time step size that correspond to the parameter values needed, as presented in Section 2.5. The simulations referred to in this section are performed in Ansys Fluent.

The complete fluid setup will consist of two solvers; one upstream fluid solver and one main solver that will connect to the System Coupling module. The upstream solver is run prior to the FSI and will act as an initialisation of the flow field.

All following contour plots, from results or in the purpose of clarifications, will be presented in the plane shown in Figure 4.2. The plane catches all the elements of the structure at once, which is beneficial when examining the flow behaviour.

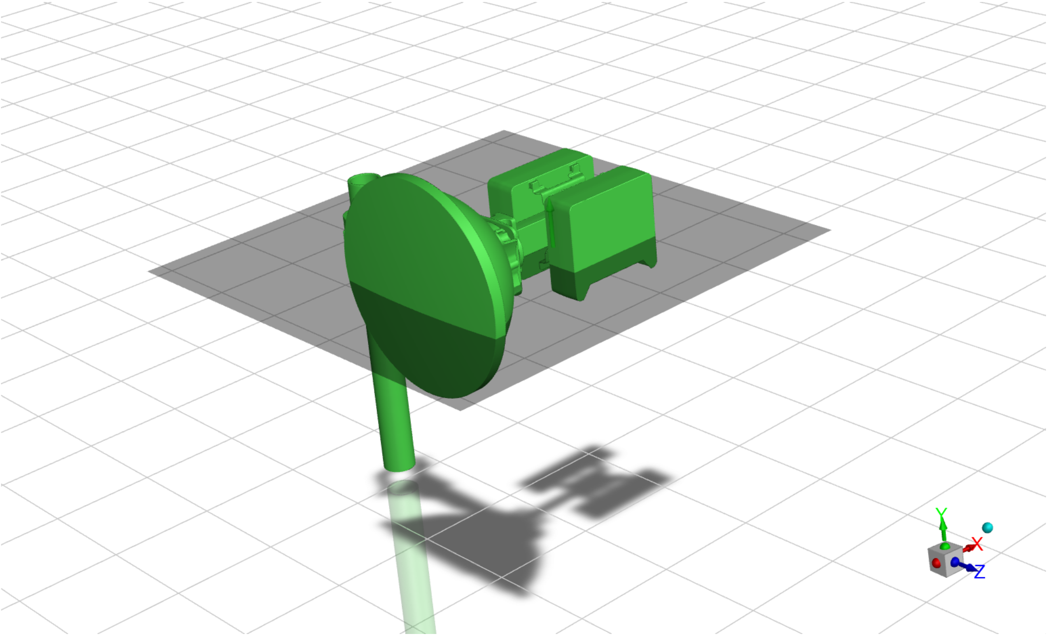

Figure 4.2: Visualisation of the plane where the following results will be presented in.

4.2.1 Mesh

The meshing is an essential part of getting a sufficient fluid domain. In turbulent areas, a fine mesh is required to capture the eddies, yet rarely desired in the whole domain. Too many cells will put an excessive load on the computation, increasing the computational time. It is always aimed to keep the cell count as low as possible, while still achieving correct results, which need to be considered during the whole process. The method used for deciding the mesh will be presented further, along with how it is evaluated.

The mesh is created in the separate module, Fluent with meshing, in Ansys Workbench, which has a built-in workflow. The workflow is called Watertight Geometry and is a straightforward step-by-step build of the mesh. The domain walls are built as a replica of the wind tunnel to ensure the flow will not differ between experiment and simulation. Inside these walls, one or more *Body Of Influence* (BOI) are created, made as a body around the structure, see Figure 4.3. The BOI's purpose is to create a sub-domain inside the large domain, to be filled with a refined mesh. It is located in the most turbulent areas of the flow, which is around the structure and parts of the wake. The BOI needs to include separation points and the turbulent areas with some margin. The margin is needed to ensure that the flow does not diffuse with the mesh, i.e., becomes mesh-dependent. This can be checked by plotting the mesh on top of the contour plot of a chosen parameter of interest and checking the behaviour.

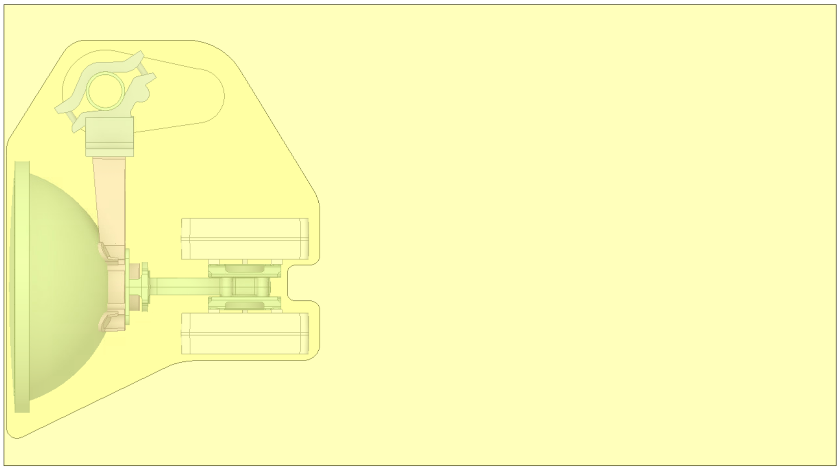

Figure 4.3: The two bodies of influence within the domain. The larger one is the shaped as a rectangle and the smaller one is following the structure more closely. The drop like shape around the pole is part of the smaller BOI. The domain walls are outside of the visual.

Volume mesh and boundary layers

The volume mesh is built with a Polyhedral-Hexahedral, hybrid structure. It uses mosaic mesh in the larger areas and polyhedral in transition areas. The mesh also included three boundary layers along the structure's surface, sized to avoid the buffer layer, see Section 2.5.1. For this project and case, the near-wall behaviour is not of great importance and therefore the y^+ value is chosen to aim beyond the buffer layer, $30 \leq y^+ \leq 300$. The sizing of the boundary layers was attained by first analytically calculating a cell height and running a RANS simulation in a fluid domain only. This generates the y^+ values near the walls, indicating if the cell height should be increased or decreased based on the goal. Then this process is done iteratively until satisfactory, by changing the first cell height, running a simulation and checking the y^+ values.

The chosen domain

As mentioned above in this chapter the geometry and walls of the domain are the same as in the experiment, see Chapter 3. It is set up with a velocity inlet, a pressure outlet and a cell count of 2.4 million cells. The fluid is defined as air at atmospheric conditions at sea level and is solved using the hybrid SBES model. The finest mesh size in the domain is found in the BOI adjacent to the structure and is 4 mm. The second BOI is larger with medium refined mesh.

4.2.2 LES evaluation

The LES evaluation is strongly connected to the mesh. This section will consider how to modify the mesh to ensure the LES has a proper resolution. The mesh has to be fine enough for it to capture the turbulent behaviour, yet not too fine, since that would mean excessive computational load. To see how the mesh size and resolution correlate more specifically, see Section 2.4.2. The LES area is located around the structure and in the wake shown in Figure 4.4. The figure shows where RANS and LES are active within the hybrid SBES model. The LES part shows up in blue and RANS in red, with the values 0 and 1 respectively. In the LES area, the BOI is located where the refined mesh will be located inside. The LES need a finer mesh size than RANS.

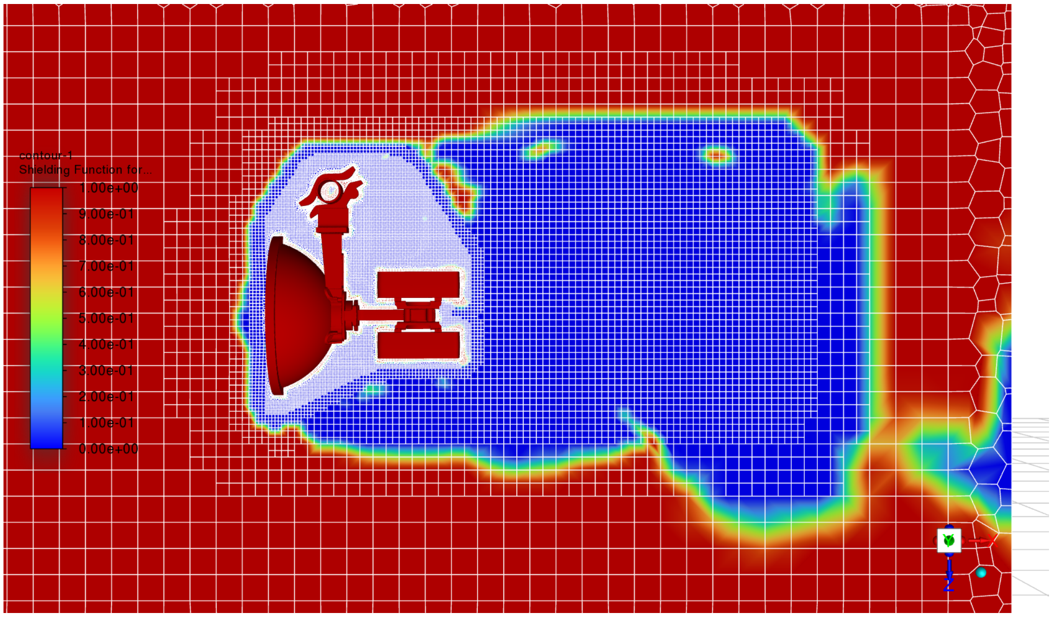

Figure 4.4: Contour plot of the SBES model. LES is represented by blue and RANS by red, with the value 0 and 1 respectively. Other colors are applied in transition regions.

The process started with an estimation of size based on a RANS simulation run. The results obtained will be time-independent, as the theory gives for a RANS simulation. From this, the integral length scale, Section 2.4.3, can be calculated with a customised field function within the software. This length scale is used as a guide to choosing the mesh size. After changing the mesh size, the same simulation is run once more to ensure it was indeed sufficient.

The process is then continued by performing the hybrid SBES simulation, still only with a fluid solver. The flow will now get the more characteristic turbulent behaviour with vortices in the air around the structure and wake. This hybrid model is time-dependent, unlike the RANS model. Due to the flow fluctuating with time, it is now necessary to sample data during the simulation to collect results for a larger range of time. The data sampling is performed when the simulation has reached a stable behaviour in the fluctuationss.

With the data obtained from the sampling, the LES resolution can be estimated and presented in a contour plot. This can be done in two ways. Either by creating a custom field function for the resolved TKE, k_{res}, as in equation (2.13) or by using the *Beta features* of Ansys Fluent. The two different methods are shown as contour plots in Figure 4.5 and 4.6. For both these cases, the theory of 80% resolution should be applied. Therefore the figure shows the range 0.8–1, where everything between 80–100% resolution is displayed. The two figures are similar in resolution, but not identical.

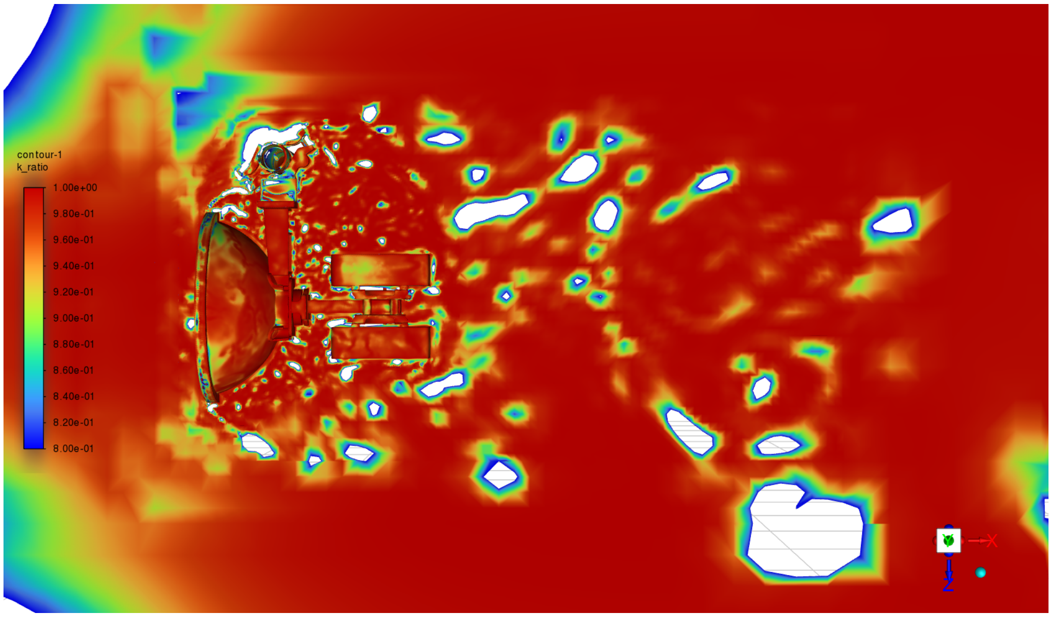

Figure 4.5: LES resolution calculated manually within the software, range 0.8–1

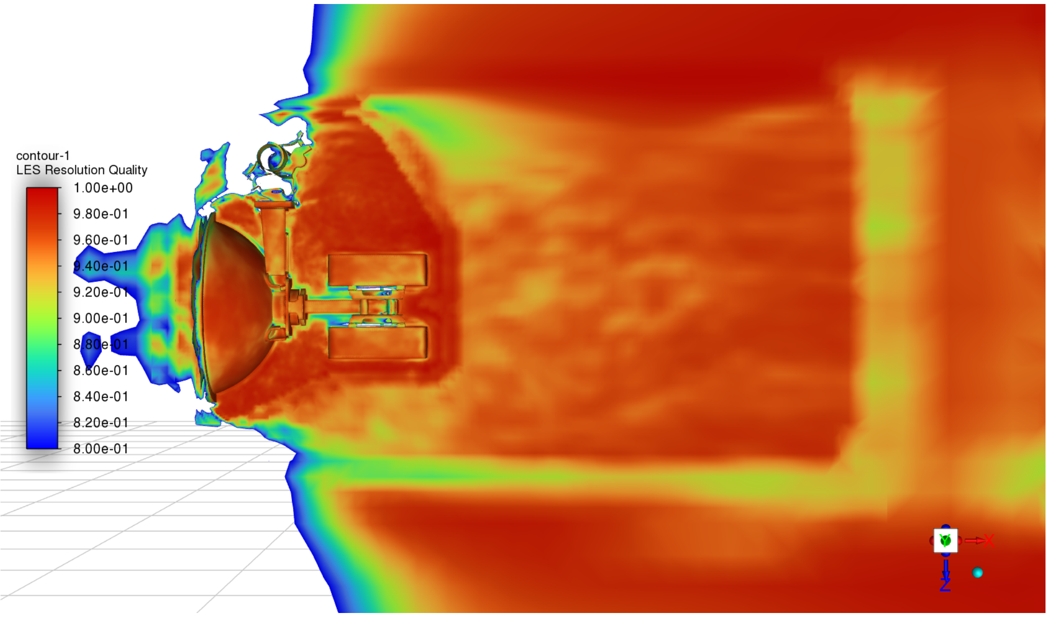

Figure 4.6: LES resolution with Ansys LES Resolution Quality, range 0.8–1

The manually calculated field (via Custom Field Functions) looks more patchy, behind the antenna and in the wake, than the Ansys LES Resolution Quality does. It has more of a smooth solution, yet a larger field in front of the antenna that isn't captured. This area is not of interest for the LES resolution analysis, since it is solved with RANS as we see in Figure 4.5 and 4.6. Both these contour plots are based on the same theory of how much TKE is resolved. The exact components of the Ansys LES Resolution Quality equations have not been confirmed, since it is not published by Ansys. Therefore it has some unknown certainties, even though the baseline theory is known. It can be of interest to do both these plots to make sure no behaviour is overlooked.

During the evaluation of these plots and seeing areas that are not fulfilled with 80%, remember to consider if that area is of importance and if the SBES model is using RANS equations in that area. In that case, the LES resolution might not need to be over the required percentage. When this part of the process is satisfied the preparations for the LES resolution are complete.

4.2.3 Time step

When choosing the time step size the theory based on eigenfrequency or the CFL number can be applied, see Section 2.5. The theory for the CFL number is useful since it is also a stability criterion. In this case, for a structure with the eigenfrequency 13.49 Hz, Section 4.1.2, the CFL method will give a smaller time step size. It is therefore the chosen method to proceed with and resulted in a time step size of 1E-4 s. The simulations will reach for a CFL number below one.

When using a hybrid model as the SBES the time-stepping needs to consider the most demanding of the two models within the hybrid. In this case, it is the LES. To get an estimation of the size, equation (2.22) can be calculated locally. This equation will not be completely accurate since it is simplified to 1D and this setup is in 3D. The estimation is used as a guiding value. This process will also be iterative and relies on trials until a sufficient time step is achieved. After an SBES run, the software obtains a contour plot of the CFL as a result. This is plotted to examine the value in all critical areas, as shown in Figure 4.7. To check the CFL, the range 0–1 is chosen in the contour plot and will show all CFL values below one. The voids in the contour plot will represent what is beyond the chosen range and therefore areas where the CFL number is not sufficient. The range between 2–5 can be observed to check if the voids are close to 1 or further away, as an indication of how much the time step should be altered. As usual with plots like these, one needs to evaluate what areas are critical and if the voids can be overlooked.

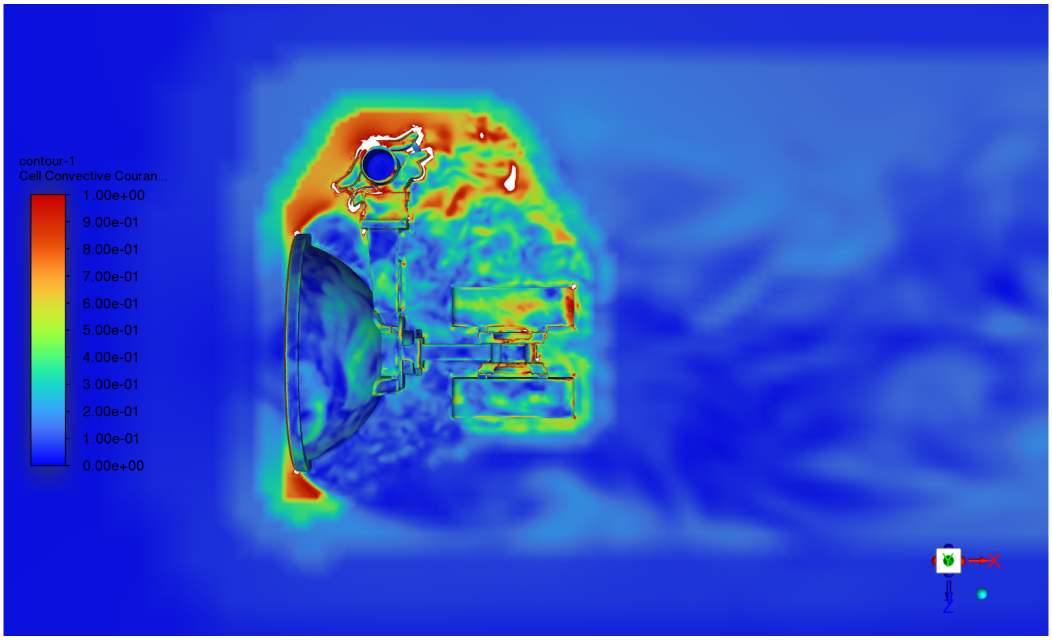

Figure 4.7: An example of a CFL plot from a Fluent simulation, showing $CFL \leq 1$*.*

4.3 The two-way FSI

Once both the mechanical solver and the fluid solver are set up accordingly, they are connected using the System Coupling module in Ansys Workbench. The System Coupling module is responsible for the data transfer between the two solvers, i.e., it transfers the force from the fluid solver to the mechanical solver, and the displacement from the mechanical solver to the fluid solver. In the settings, the time step size for the two-way FSI is decided as well as the number of coupling iterations. The default number of coupling iterations is five. However, by checking the convergence it is possible to lower the number if both solvers converge at earlier iterations to save computational time.

When the simulation is complete, the obtained data can be processed and analysed. The variables of interest for this project are mainly the displacement and vibrations of the antenna, but other data, such as velocity and pressure, can be used to understand and validate the results. The extracted displacement data is then compared to the displacement obtained from the wind tunnel testing and is presented and discussed in Section 5.2. The complete process that has been presented in the previous chapters is visualised in Figure 4.8. The CAD is somewhat overlooked in the process since it is quite trivial in the context. Even so, it is the initial step of the process and the geometry is used in both the structural and the fluid setup. The process continues with the preparation steps Modal and Damping for the structural setup, and Fluent with meshing in the fluid setup. Fluent with meshing is the initialisation of the fluid flow, mentioned in Section 4.2. The main FSI part is highlighted in the figure and refers to the acting components in the coupling/data transfer, which are active while running the simulation. EnSight is the post-processing step where the animations are created and the FSI results are analysed. Post-processing can also be done separately in Mechanical and Fluent, but it will only show the separate solver's solutions.

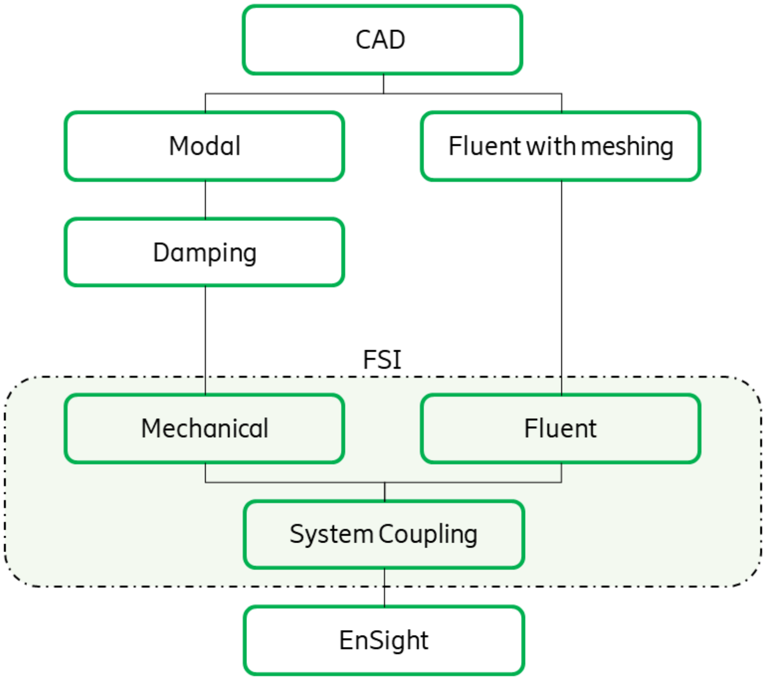

Figure 4.8: Flow chart of the final process for setting up the FSI. Containing the preparation steps, the actual FSI and the post-processing step.

4.4 Decreasing the computational time

The two-way FSI described previously in this chapter is set up in a way that is supported by the theory and all parameters are chosen very thoroughly and carefully. However, in the industry, it is important to optimise the process and save computational time without losing too much accuracy. The definition of ”too much” of course differs and can be hard to determine. In this case, the variables of main interest are deflection and force. The results of these variables will be used for comparing the accuracy of the optimised setup.

The most straightforward way to decrease the computational time is to increase the time step size. Compared to the fine time step size derived from the Fluent simulation of 1E-4 s, a larger time step size was chosen. This time step size is five times larger than the fine time step size, i.e., 5E-4 s. This time step corresponds to 150 steps per period, which is still more than the recommended 70–100 steps for an FSI.

It is important to keep in mind that changing the size of the time step interferes with other parameters, such as the CFL number. The new time step size resulted in a CFL number in the range of 0–10, compared to 1–2 for the fine time step size, see Figure 4.9. Even if a CFL number less than 1 is desired for the stability criterion, studies suggests that a larger number is not necessarily an issue as long as the solution converges [22][17].

When increasing the time step size, it became evident that the simulation would require either more

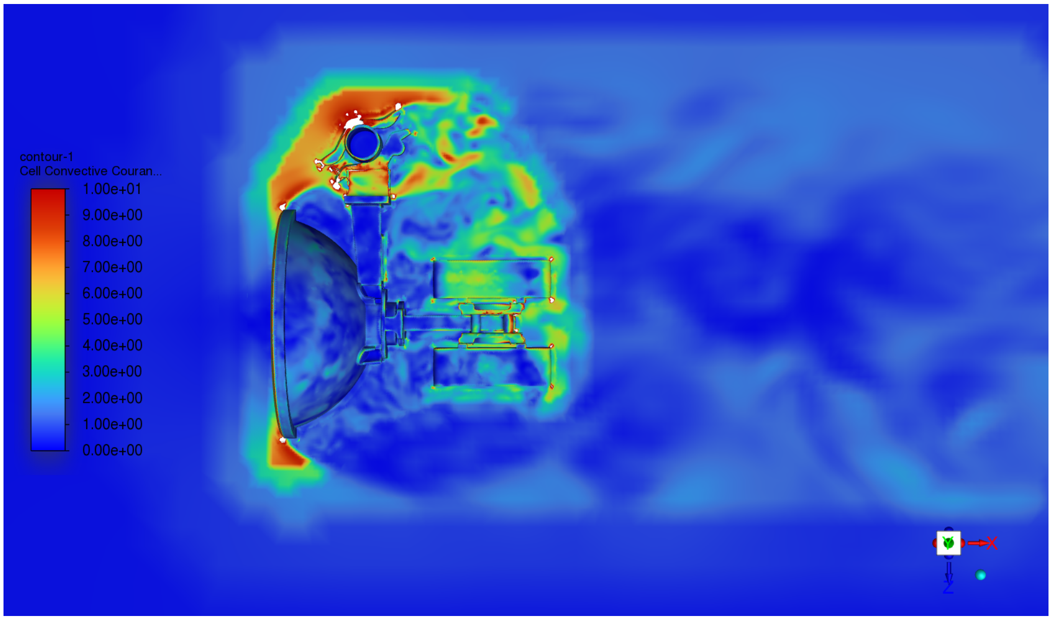

Figure 4.9: Contour plot of the CFL number for the larger time step size of 5E-4 s. The CFL number range from 0–10, with the higher values centered around the pole.

internal iteration for the CFD solver or more coupling iterations in the System Coupling module in order for the solution to converge. To ensure a converged solution, the residuals are observed and checked that they reach set convergence criteria. In addition, a force data plot is observed during the simulation to ensure that the fluent solution in each time step is converging. Increasing either of the internal iterations in Fluent and the coupled iterations in System Coupling will also increase the computational time. Therefore, it is important to make sure that the time saved by increasing the time step size and the time lost from the increased number of iterations do not cancel each other out.

In this case, increasing the number of internal iterations in Fluent proved to be the more efficient way since the Mechanical solver already converged in each time step. 18–20 internal iterations were necessary for this case to ensure that the CFD solution converged.

When solving for the turbulent flow, since part of the flow is modelled, two simulations can produce different results even with the same settings. To make sure that a simulation with an increased time step size, apart from ensuring convergence in each time step, gives accurate results, it is useful to look at the parameters of interest. A comparison in deflection using the finer time step size versus the larger time step size is presented in Section 5.3.

5

Comparison

The most important part of the project is to compare the experimental and simulated results. This is where conclusions can be drawn and give an indication of how well the two correlate. The results presented in the previous chapters will be compared and analysed.

5.1 Damping ratio between simulation and experiment

As previously stated in Table 3.3, the average damping ratio using Approach 1 and 2 for the method of logarithmic decrement, was 4.58% and 2.78%, respectively. This ratio was calculated using experimental data from the wind tunnel testing and is therefore only valid to the physical model, i.e., not necessarily the same damping ratio as for the simulation model.

In Section 4.1.3, the drag-and-drop test was described as a way to mimic the hammer impulse test from the wind tunnel experiment. The damping ratio that yields the same displacement as for the experiment connects the physical model to the computational model.

The comparison between the simulation and the experimental data using the damping ratios calculated using Approach 1 and 2, Section 3.4.1, can be observed in Figure 5.1. To reach the desired initial displacement of 0.92 mm, a force of 106.6 N was required for both simulations. The force was applied to the same location as the hammer impact, in this case the backside of the radio. As can be observed in the figure, both cases underpredicts the second and the third amplitude peaks. In Figure 5.1a, the simulation continues to have a lower amplitude compared to the experimental data, suggesting that the damping ratio of 4.58% is too high for this model. The results from Figure 5.1b is harder to interpret since it starts with a lower amplitude than the experiment, matches agreeably well and finally overpredicts the amplitude. It is important to keep in mind that since the antenna structure is mounted asymmetrically, i.e., mounted on pole to the side, an impact from behind will result in momentum being created and the movement will not be straight back-and-forth in the x-direction. Instead, it will move in a more or less circular motion, grounded by the pole.

Apart from comparing the amplitudes, it is of interest to compare the frequency at which the curves oscillate. As previously mentioned in Section 3.4, the frequency from the experimental data was calculated to be 12.3 Hz. From the conducted modal analysis, the eigenfrequency of the first mode of the simulation model was found to be 13.49 Hz, see Table 4.1. It is therefore reasonable that the simulation curve oscillates at a slightly faster rate which is more noticeable as time goes on.

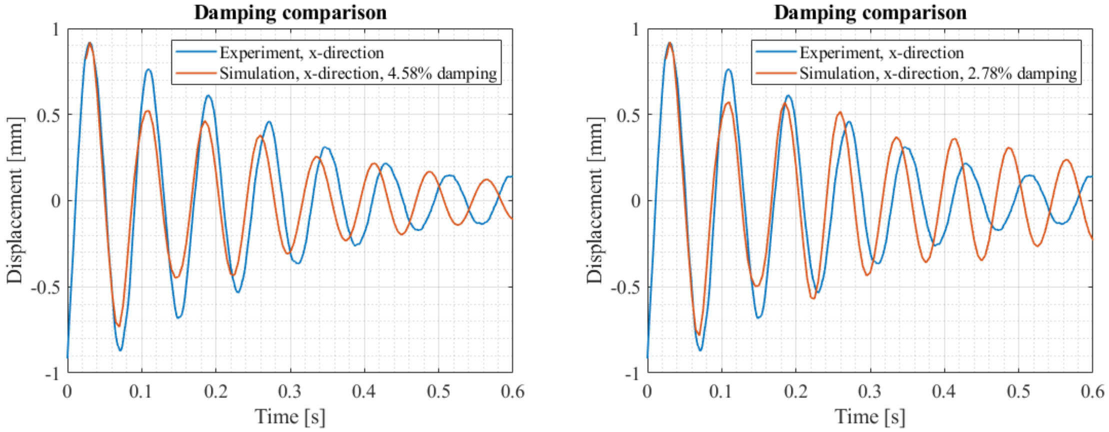

(a) Damping ratio of 4.58% *(b) Damping ratio of 2.78%*

Figure 5.1: Comparison between the hammer impulse test with the backside radio as impact location and the drag-and-drop test from the simulation. The simulations use the calculated damping ratio from the method of logarithmic decrement which resulted in a damping ratio of a) 4.58% and b) 2.78%. The force required for the initial displacement of 0.92 mm was 106.6 N for both cases.

It can be concluded, from the results in Figure 5.1, that the damping ratio of 2.78% is better suited for the simulation out of the two calculated damping ratios, and is the damping ratio chosen to proceed with when conducting the simulation with a constant wind load. Ideally, a more detailed study investigating damping ratios around 2.78%, to find which ratio would give the best match, would be conducted. This was not possible in this project due to time constraint. For further comparison of damping ratios, it is interesting to see the results of a case with no damping, which can be observed in Figure 5.2a. In the figure, the oscillations does not steadily decrease in amplitude. Instead, the peaks increase and decrease during the time span in an unpredictable manner that is probably due to movement in other directions occurring simultaneously.

The final comparison of damping ratio, by tweaking the simulation to match the experiment to the best ability, can be observed in Figure 5.2b. The previously presented comparison of damping ratios all had the initial force of 106.6 N. In this case the initial force was increased to 180 N and the damping ratio was set to 7%. As can be observed in the figure, the initial peak does not match the experimental peak, but the following peaks follow the amplitude of the experiment nicely. The conclusion drawn from this observation is that there seem to be differences in the experimental initial data that are not captured by the simulation, e.g., the influence of the second eigenmode. This makes it difficult to decide on a specific damping ratio. Ideally, recreating the hammer impulse test with a known force, or conducting a physical drag-and-drop test would be beneficial for validating the damping ratio. This will be discussed further in Section 6.1.

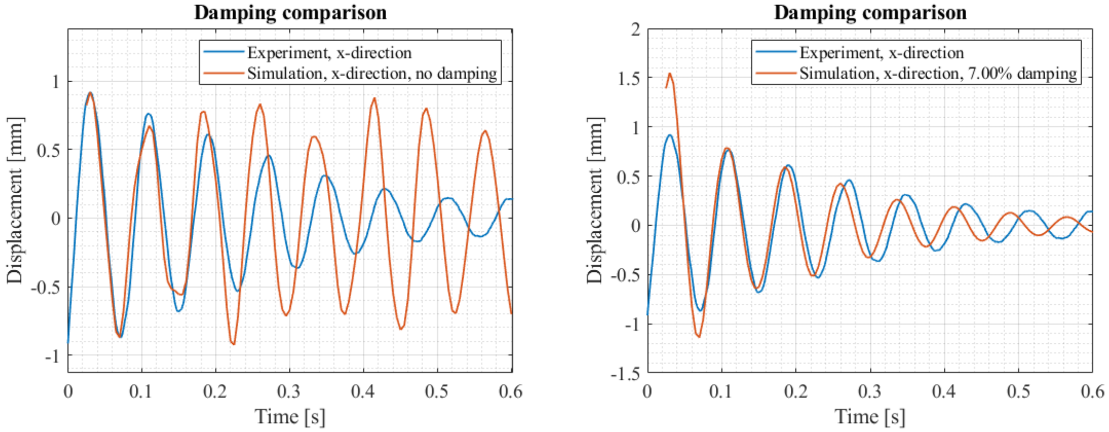

(a) Damping ratio of 0%

(b) Damping ratio of 7%

Figure 5.2: Comparison between the hammer impulse test with the backside radio as impact location and the drag-and-drop test from the simulation. a) 0% damping ratio and b) 7% damping ratio. The force required for the initial displacement was 106.6 N for the simulation with no damping and 180 N for the simulation with 7% damping.

As previously mentioned, the damping ratio 2.78% was chosen to proceed with. In this project, the interest lies in the behaviour of the deformation when an antenna is subjected to a wind load and not an impulse. The deformation will not necessary subside as it did for the drag-and-drop tests. Instead, the constant wind load could be compared to the antenna being constantly hit by impulses and it is therefore difficult to predict the impact of the damping ratio. This is further discussed in the next section, where the comparison of displacement under constant wind load is made.

5.2 Displacement under constant wind load

The comparison between the experimental result and the result from the simulation is presented below. It is for the case with a constant wind load of 40 m/s with an incoming angle of 0°. The comparison is limited by the experimental data which has a total measured time of 0.35 s, whereas the simulation has a total time of 1 s. Because of this limited data, it is difficult to deduce if there is a pattern or if the behaviour is random. Since the data from the experiment was measured after the wind load in the wind tunnel had stabilised and the antenna had been subjected to the wind for some time, there is no settling time. The numerical simulation however, does have a settling time where the amplitude in the beginning is higher than the settled oscillations.

The first thing to notice in the following comparisons is that the deformation is much larger in the x-direction compared to the y-direction. This is to be expected since the x-direction correlates with the direction of the incoming wind and the antenna structure will deflect more in that direction. The deflection in x-direction is also more uniform than the data in y-direction, meaning that it is harder to know if certain peaks are correlating to the experimental data. Therefore, when shifting the results from the simulation, the deflection in y-direction has been the deciding factor.

As can be observed in Figure 5.3b, there are sometimes double-peaks in both the simulation data and the experimental data, e.g., at 0.15 s for the experimental data and 0.4 s and 0.6 s from the simulation. By shifting the experiment curve 0.225 s in time and aligning the experimental data to the first double-peak of the simulation, see Figure 5.4b, one can see that the curves correlates quite well in y-direction. As with any experiment, an exact correlation is not to be expected, but looking at the amplitude of the curves and the frequency, the simulation replicates the behaviour of the experiment well.

Since the amplitude of the oscillations vary over time in both the experimental data and the results from the simulations, it is difficult to make a direct comparison. Comparing the range between the maximum value and the minimum value gives an indication if the movement of the antenna is captured. The range between the maximum value and the minimum value for the experiment in x-direction when shifted 0.225 s, see Figure 5.4a, is approximately 1.7 mm, whereas it is approximately 1.4 mm for the simulation. In y-direction for the same shift in time, see Figure 5.4b, the range between the maximum value and the minimum value is approximately 0.6 mm for the experiment, and approximately 0.5 mm for the simulation. The ranges between the experiment and the simulation are agreeable. However, as previously mentioned, the simulation has a settling time where the amplitude continues to decrease up until approximately 0.4 s. It is therefore reasonable to shift the comparison to not include the first 0.4 s of the simulation result.

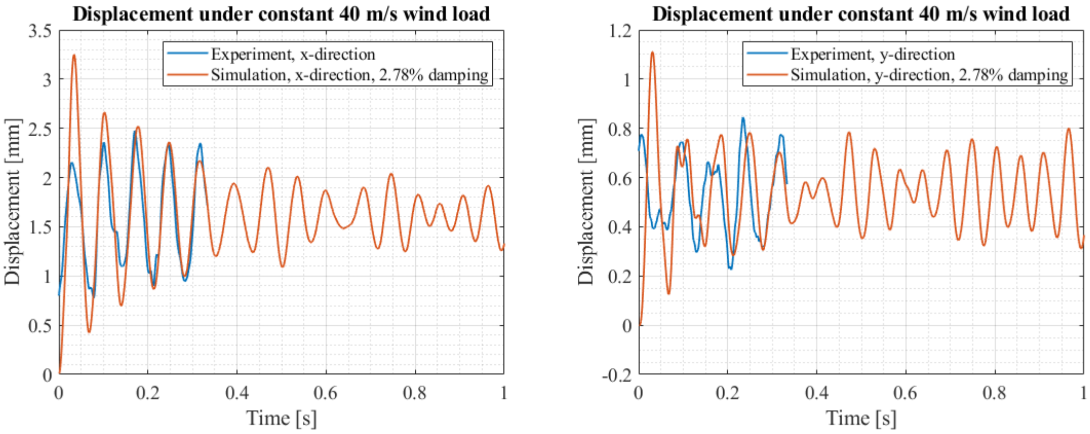

(a) Displacement in x-direction

(b) Displacement in y-direction

Figure 5.3: Comparison of the displacement of the antenna in a) x-direction and b) y-direction between experiment and simulation. The simulation had a damping ratio of 2.78%.

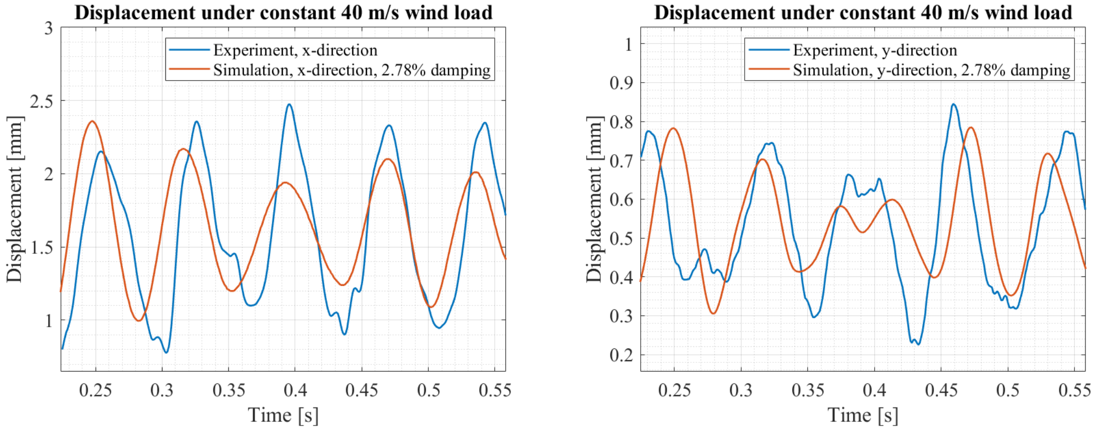

(a) Displacement in the x-direction

(b) Displacement in the y-direction

Figure 5.4: Comparison of the displacement of the antenna in a) the x-direction and b) the y-direction between experiment and simulation with the experiment shifted 0.225 s in time. The simulation had a damping ratio of 2.78%.

In Figure 5.5a and 5.5b, the experimental curve has been shifted 0.45 s in time to once again align the double-peaks in the y-direction. As can be observed from the figures, the amplitudes does not match as well in the x-direction as it did when the experiment was shifted 0.225 s. This means that when the simulation has settled, it underpredicts the vibrations of the antenna. This is further discussed in Section 6.

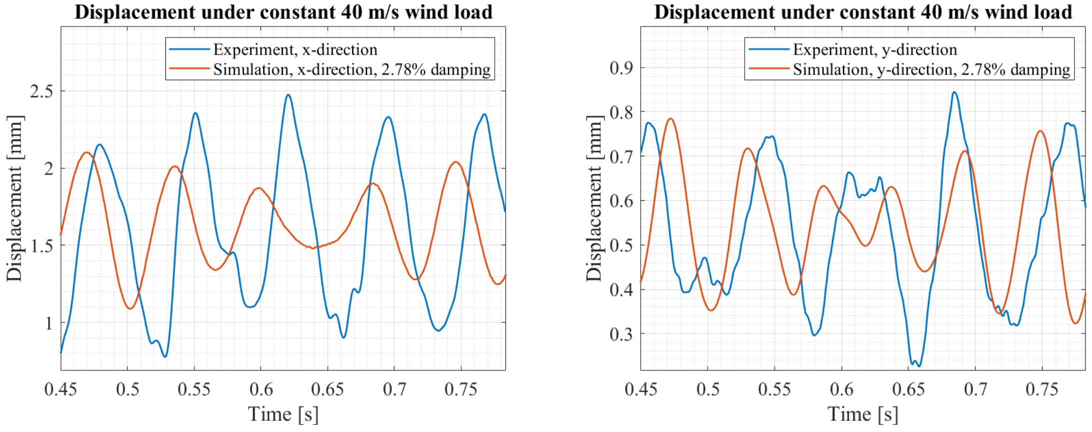

(a) Displacement in the x-direction

(b) Displacement in the y-direction

Figure 5.5: Comparison of the displacement of the antenna in a) x-direction and b) y-direction between experiment and simulation with the experiment shifted 0.45 s in time. The simulation had a damping ratio of 2.78%.

Knowing that the simulation and the experimental data match fairly well in frequency and moderately well in amplitude validates the process and gives reliance that other parameters of interest can be extracted from the simulation, e.g., pressure, velocity fields and other parameters.

Since the simulation with the damping of 2.78% seemed to underestimate the structure's displacement, a case with no damping was performed. The results of this simulation are shown in Figure 5.6. Unlike the damped cases, the undamped curve did not have a settling time. The full curve can be found in Appendix A.4. The frequency seems to correlate close to the damped simulation and the experiment, but overestimates the displacement. No real structure is free of damping, there will always be some damping in material and structure. Therefore, this case is unrealistic and is not expected to match. It is rather simulated as a way to understand the impact of the damping.

As can be observed in Figure 5.6b the undamped simulation curve displays much more noise and irregularities than the damped simulation and experiment. It is hard to distinguish a concrete pattern of the curve, and thus more difficult to analyse.

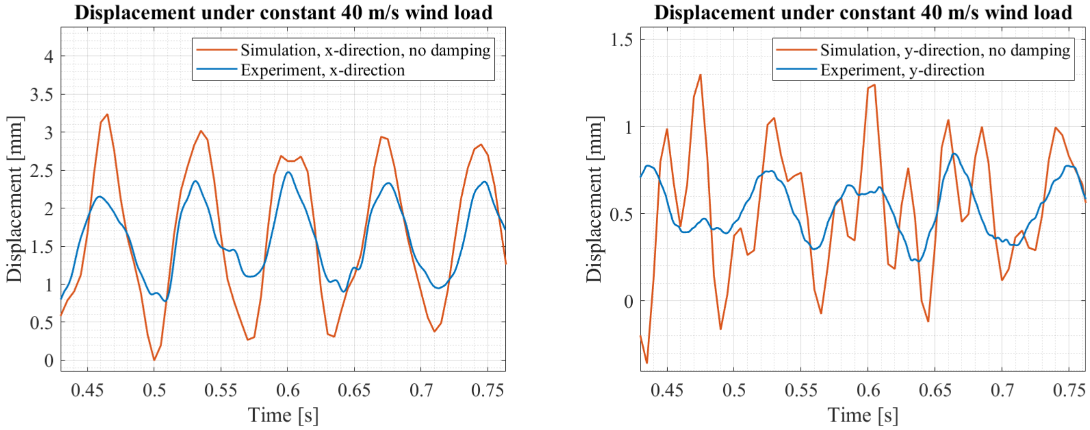

(a) Displacement in the x-direction

(b) Displacement in the y-direction

Figure 5.6: Comparison of the displacement of the antenna in a) x-direction and b) y-direction between experiment and undamped simulation with the experiment shifted 0.43 s in time.

5.2.1 Average amplitude magnitude

In this section the average amplitude magnitude of peaks from the experiment and the simulation are presented. The average amplitude from the simulations are measured after the time 0.4 s, in order to exclude the higher amplitudes from the settling time.

The average amplitude magnitude in the x-direction for the experiment and the simulation can be observed in Figure 5.7. For the experiment the displacement is approximately 2.3 mm and for the simulation it is 1.9 mm, meaning that the difference is 0.4 mm. The same comparison, for the y-direction, can be found in Figure 5.8, where the experimental amplitude magnitude is 0.74 mm and the simulation amplitude magnitude is 0.70 mm. This results in a difference of 0.04 mm.

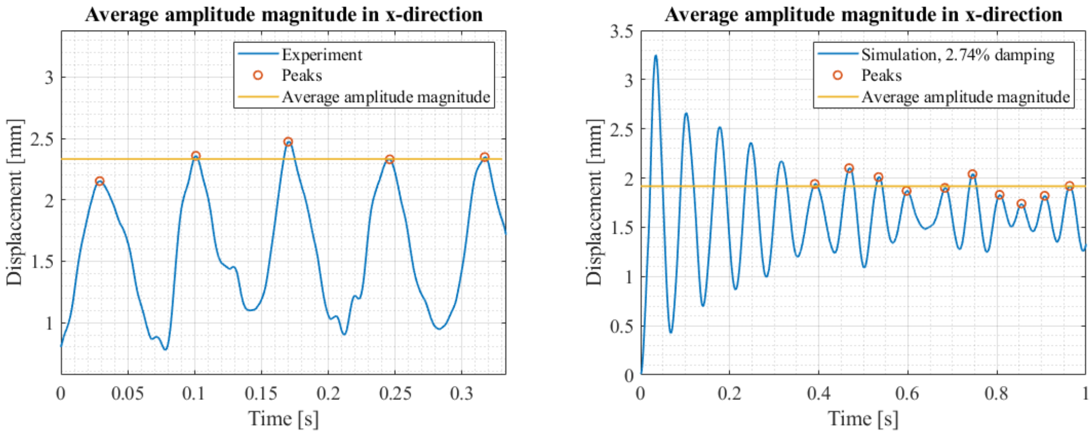

(a) Experiment, x-direction

(b) Simulation, x-direction

Figure 5.7: Average amplitude magnitude in the x-direction from (a) the experiment of 2.3 mm and (b) the simulation of 1.9 mm.

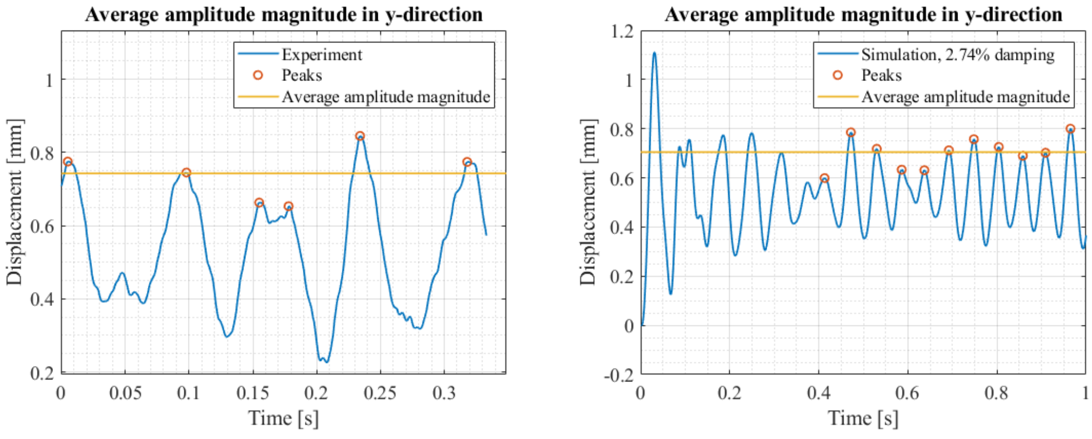

(a) Experiment, y-direction

(b) Simulation, y-direction

Figure 5.8: Average amplitude magnitude in the y-direction from (a) the experiment of 0.74 mm and (b) the simulation of 0.70 mm.

In addition to the comparison of average amplitude magnitude, it is of interest to compare the maximum and minimum displacement, see Table 5.1. The difference in maximum and minimum displacement in x-direction between the experiment and the simulation are 0.3 mm and 0.32 mm respectively. In y-direction, the difference in maximum and minimum displacement between the experiment and the simulation are 0.05 mm and 0.08 mm respectively.

Table 5.1: The maximum and minimum displacement for the experiment and the simulation in x and y-direction.

	Max	**Min**
Experiment x-direction	2.47 mm	0.78 mm
Simulation x-direction	2.17 mm	1.10 mm
Experiment y-direction	0.85 mm	0.23 mm
Simulation y-direction	0.80 mm	0.31 mm

The critical aspect of this is the maximum displacement, since that will diverge the transmitted signal the most. To evaluate how much the simulation deviates from the experiment, the following ratios are calculated:

Maximum displacement in x-direction

$$\frac{Simulation}{Experiment} \approx 0.879 = 87.9\%$$

Maximum displacement in y-direction

$$\frac{Simulation}{Experiment} \approx 0.941 = 94.1\%$$

This means the maximum peak amplitude, i.e., the largest displacement, is underpredicted in the simulation in both directions.

As previously mentioned, a case with no damping was simulated. The undamped case is of interest to see how much impact the damping ratio has on the displacement of the antenna. Similarly to how the average amplitude magnitude was calculated for the experiment and the simulation with 2.78% damping, the results from the undamped case can be observed in Figure 5.9. The average amplitude magnitude for the undamped simulation was found to be 2.86 mm in the x-direction and 0.74 mm in the y-direction.

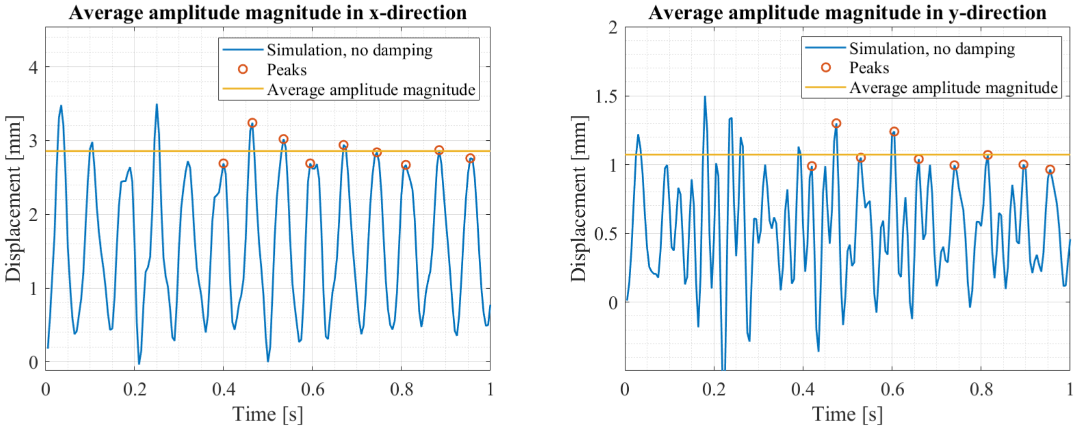

(a) Undamped simulation, x-direction

(b) Undamped simulation, y-direction

Figure 5.9: Average amplitude magnitude for the undamped simulation (a) the x-direction of 2.86 mm and (b) the y-direction of 0.74 mm.

The maximum and minimum displacement of the undamped simulation can be found in Table 5.2. Comparing the maximum displacement of the simulation to the experiment gives a difference of 0.5 mm in the x-direction and 0.45 mm in the y-direction. In both directions, the undamped simulation has a larger maximum displacement.

Table 5.2: The maximum and minimum undamped displacement for the experiment and the simulation in x and y-direction.

	Max	**Min**
Experiment x-direction	2.47 mm	0.78 mm
Simulation x-direction	3.24 mm	-0.0036 mm
Experiment y-direction	0.85 mm	0.23 mm
Simulation y-direction	1.3 mm	-0.36 mm

Again, to evaluate how much the simulation deviates from the experiment, the ratios are calculated:

Maximum displacement in x-direction

$$\frac{Undamped\ Simulation}{Experiment} \approx 0.879 = 131\%$$

Maximum displacement in y-direction

$$\frac{Undamped\ Simulation}{Experiment} \approx 0.941 = 153\%$$

This means that the undamped simulation overpredicts the displacement more than the dampened simulation underpredicts the displacement.

5.3 Time step size

The comparison between two time step sizes, as mentioned in Section 4.4, can be observed in Figure 5.10. The fine time step size, 1E-4 s, and the larger time step size, 5E-4 s, are compared in both the x-direction and the y-direction, see Figure 5.10a and 5.10b respectively. A common way to compare computational time is to multiply the hours it took for the simulation to finish with the amount of cores used. This resulted in 7200 core-hours for the fine time step size and 2400 core-hours for the larger time step size, which in this case took 15 and 5 days respectively.

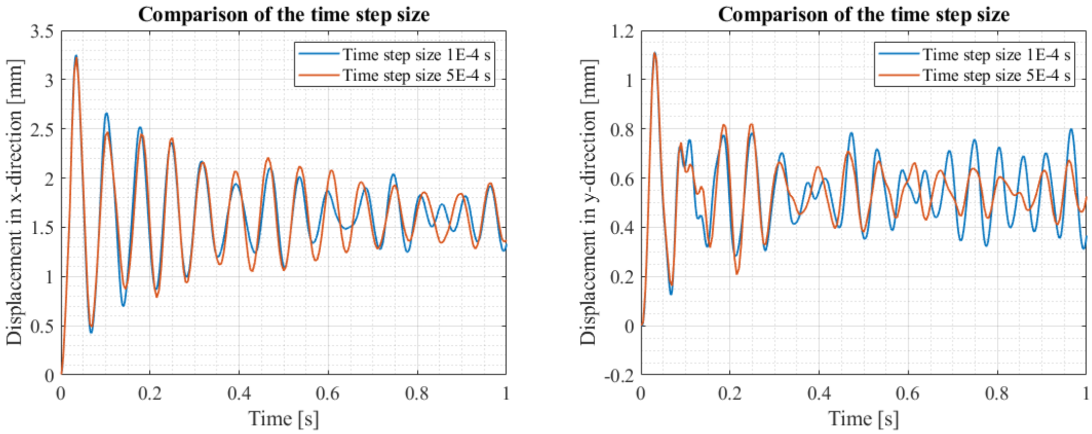

(a) Displacement in the x-direction *(b) Displacement in the y-direction*

Figure 5.10: Comparison between the simulation run with the fine time step size of 1E-4 s and the larger time step size of 5E-4 s. (a) Displacement in the x-direction and (b) displacement in the y-direction.

For both figures, the first oscillations of the curve correlate very well. From 0.4 s they start to differ, especially in the y-direction where the larger time step curve has a trend of lower amplitude. That is where the large difference lies between these time step sizes. To clarify, if the simulation was run with identical settings twice, we could expect different shapes of the curves. Instead, trends and amplitude are evaluated. The x-direction is the one with the largest deviation in deflection of the two curves.

6

Discussion

The objectives presented in the introduction of this report will now be discussed to see if the goals were met. Following this chapter, we will discuss the experimental testing from the wind tunnel and the results obtained for the damping ratio. This is followed by a discussion about the validation of the results and the simulation process and finally ends with a section about improvement and suggestions for future work.

6.1 Wind tunnel testing and experimental data

In Chapter 3, the wind tunnel testing is described. The data obtained from these tests is of utmost importance since it validates the process developed in this project. Four different cases with constant wind load as well as three hammer impulse tests were conducted, described in Section 3.2. The wind tunnel testing was conducted at the beginning of the project and required intricate planning which was made before knowing which results would be important for the validation.

Knowing what we know now, it would be interesting to run the cases with constant wind load over a longer time. The measured data used in this project covered a time of 0.35 s which is not enough to surely say if there is a repeatable pattern in the movement of the antenna structure. For comparison, the total time from the simulation was 1 s. Apart from this, the data obtained from the cases with constant wind load was measured in such a way that if we were to conduct the experiments all over again, we would not change the setup. However, the same can not be said for the hammer impulse tests. Even though the hammer impulse tests gave some good results which were used for the spectral analysis and the calculation of the damping ratio, the tests can not be recreated. This is due to the difference in impact force and direction from the hammer impact due to human error. The hammer impulse test with the location of impact on the top mast did not give good results since the direction of the hammer impulse mainly was in the z-direction, which was not captured by the high-speed camera.

In hindsight, it would have been better to do these hammer impulse tests as a drag-and-drop test, similar to the one recreated in the simulation, see Section 4.1.3. Instead of hitting the antenna with a rubber hammer, it would be better to displace the antenna at a known distance or find a way to ensure that the hammer struck the antenna with a known force and fixed direction. Knowing the initial force would be helpful in the comparison between the calculated and the simulated damping ratio.

On a final note, even if the hammer impulse test could be improved, it still gave a good indication of the eigenfrequencies of the structure. The test can also be conducted in the industry as long as there is a way to capture the displacement, e.g., by using a high speed camera. Knowing the eigenfrequency of a structure is a good starting point when conducting these types of simulations.

6.2 Damping ratio

It is well-known that the effects of damping are rather difficult to get to match between a mathematical and a physical model. In this project the damping ratio was calculated using two different methods, namely the method of logarithmic decrement, Section 2.3.1, and the half-power bandwidth method, Section 2.3.2. Both methods use data from the experimental testing and, as previously discussed, should give the structural damping ratio for the physical model. The displacement of the antenna did not show a steady decrease in amplitude, instead, an interfering second mode could be distinguished. This raised the question of how to apply the method of logarithmic decrement, and we came up with two approaches. Approach 1, where all peaks were used, including those where the second mode affected the amplitude, was not successful and gave scattered results. Approach 2, focusing on an interval where the amplitude decreased steadily proved to be a better way and resulted in a more narrow range of values. Ideally, the damping ratio of the structure should give the same value regardless of direction and it would be of interest to apply this approach to more experimental data to see if the results would gather around a certain value.

The half-power bandwidth method did not work for the data obtained from the hammer impulse tests since the points from the spectral analysis were sparse. This resulted in different damping ratios for all the cases scattered over a wide range. The half-power bandwidth method requires a smoother curve, i.e., more data points to ensure that the peak values and the half-power points are true to the frequency. There is a reason why this is a common method and with the right tools, this could be a good method for finding the damping ratio. However, in this case, with the hammer impulse test, it did not provide consistent results.

The challenge of finding the correct damping ratio of the structure was not finished after calculating it from the experimental data. Instead, we were met with several possible approaches for defining the damping in the simulation. To complicate matters further, it is possible to enter a structural damping as well as numerical damping. In this project, we chose to focus on structural damping and leave the numerical damping as the default setting in the mechanical solver. The method chosen for the damping ratio was to define the damping ratio and the dominant response frequency, in this case, the first eigenmode.

When verifying the damping ratio against the experimental data as presented in Section 5.1, there were different ways to run the drag-and-drop simulation. We chose to use a method called the Full-transient method, which is the most accurate method, but also the most time consuming one. Other methods such as Mode superposition (MSUP) and Constant structural damping coefficient (DMPSTR) were investigated to save computational time, but in the end, the accuracy of the displacement was the most important. In conclusion, there is more work to be done in order to fully understand the effects of the damping ratio and how to accurately insert it into the simulation setup. Even so, it is very common in the industry to use an arbitrary damping ratio for a structure and run with it. In other words, it is unusual to do this kind of damping study using experimental data to the extent that is done in this project. Instead, by including a very small damping ratio, one could argue that the results from the simulation will overpredict the displacement and thus be on the conservative side.

6.3 Evaluating results

For the simulation setup, many aspects can be discussed and argued for, since there are numerous ways to set up a fluid and a structural domain with the software. For example, there were many settings within the software that we did not have time to investigate, settings that might help the simulation perform better, faster or more reliably.

If we look at the results received from Section 5.2, they are quite satisfactory. Both frequency and amplitude agree better than we expected them to. We see the same trends with the double-peaks in the displacement curves, which we initially thought was noise that would be overlooked by the simulation. The damped displacement is smaller than the experiment, but this is somewhat expected. Since the structure uses simplified contact areas instead of the true bolts and screws that hold it together, we do expect the structure to become stiffer and in turn, show less displacement. Material parameters and centre of gravity are the main factors that need to be accurate to the physical model for the damping to match. Despite the decreasing amplitude of the displacement curve, the average amplitude magnitude still correlates decently.

The case of no damping, in turn, overestimates the displacement, which again is expected. Since all structures have some damping, the case of no damping is an unrealistic behaviour. We wanted to observe the results merely because it gives a form of baseline for the simulated results. In an ideal case, several simulations with different values of damping ratio would be conducted to see how far off the 2.78% damping ratio was. That did not fit within the time frame of the project. Without damping, the solver became much more unstable and required more iterations per time step and a Fluent solver method that is more robust in unsteady simulations. The FSI simulation required more attention for it to converge. This increased the computational time. In summary, the undamped case was harder to converge.

If this process of experiment and simulation were to be applied to several antenna structures, we could start to see trends of how much the simulation is underestimating. This could be used to form a safety factor that will make sure results are portraying correct displacements.

From the increased time step size, see Section 5.3, the curve is diverted from the original curve. What is interesting is that for the x-direction, it slightly increases and for the y-direction, it decreases noticeably in the second half of the time spectrum. It would be more expected for both directions to either increase or decrease simultaneously. For our case, it is most important that the x-direction stays consistent when increasing the time step size. Partly because it is the direction in which the wind is striking the antenna, but also where we have the largest displacement. This is the most important aspect of this project since that is what causes the transmitting signals of the antenna to deflect. It is also an aspect that the industry will have to take into consideration when performing this process, how much the results can be compromised to win time and effectiveness.

The simulation analysis would benefit from experimental results that included a wider time frame. The smaller time range gives us some sense of the movement and what magnitudes we are considering in displacement, but it could have additional behaviours and trends that are not observed within this range. A longer period would assure that longer trends would be captured as well. That is also true for the simulation itself, if we had a longer time to analyse we would have more certainty in the results. In this case, it was physical time and core-hours that limited us. Ideally, we would have run a several seconds long simulation, with a very fine mesh, a very fine time step size and an exact replica of the structure, to use as a baseline simulation. This was way beyond the project's capacity time-wise. Also, it is of no interest to the company to have a process that needs several weeks of simulations. It simply does not fit the industry's demands on time.

6.4 Future work

The simulation process developed in this project has the potential to lay the groundwork for future simulations and solutions concerning wind-induced vibrations of antennas. As for most things, there is always room for improvement and further development which are discussed in this section.

As mentioned in Section 6.1 and 6.3, conducting additional wind tunnel tests over a longer time would be beneficial for validation and conclusion of possible patterns in the movement of the antenna. It would also be of interest to conduct similar experiments for other antenna models to verify the simulation process further.

The most probable cause for differences between simulation and experiment is differences in the computational model and the physical model and as previously mentioned, it is hard to be certain that the models match. Parameters such as material density, stiffness, homogeneity in the components and centre of gravity of each part are challenging to establish from a physical model. Even if dimensions can be measured and data sheets contain information about the antenna, a method to confirm these parameters is missing. As previously mentioned, there is also room for further investigation concerning the damping ratio of the structure and how to best calculate it from experimental testing.

Conducting further research about optimising the time for a fast and reliable process. Since the goal in the industry is to have robust and fast results delivered to the customer within a reasonable amount of time. This can be done by evaluating how far the time step size can be increased while still offering correct results.

Finally, a method for validating the simulation results without using experimental data would be beneficial for future work where the possibility of wind tunnel testing is limited. Either that or constructing a simpler version of the experiments that are more accessible and not time-consuming for the company. This is a process that should not demand a large workload when executed.

7

Conclusion

In a world where we are more connected than ever before, larger demands are placed upon antennas and their precision, making every vibration count. The process presented in this report shows that it indeed is possible to capture the wind-induced vibrations of antennas with only numerical solvers. Of course we verified the results against experiments, but ideally with enough testing, a simulation-only process will be attained.

In our study, we found that the calculated damping ratio of the structure underpredicts the displacement of the vibrations, while no damping overpredicts it. This gives us a range within which the vibrations occur and implies that the process can be used to simulate the vibrations, as was one of the goals of the project.

When the simulation process was fully developed, a tutorial with guidance to Ericsson could be compiled, completing another one of our objectives. The industry, and more importantly the company itself, now have a full set of tools and directions for achieving similar results.

As of today, this type of detailed process is not yet common in this type of industry. The antennas of the future will have higher transmission frequencies, resulting in more displacement sensitive antennas. A smaller vibration will have a larger impact and it is no longer enough to perform static analyses. The work described in this project could be the starting point for a solution to prevent the decrease in performance as technology continues to evolve.

References

[1] "Eurocodes: Building the future - the european commission website on the eurocodes." [Online]. Available: https://eurocodes.jrc.ec.europa.eu (Accessed: 2022-05-10).

[2] "En 1991-1-4 (2005): Eurocode 1: Actions on structures - part 1-4: General actions - wind actions." [Online]. Available: https://www.phd.eng.br/wp-content/uploads/2015/12/en.1991.1.4.2005.pdf (Accessed: 2022-06-13). Authority: The European Union Per Regulation 305/2011, Directive 98/34/EC.

[3] Y. Bazilevs, K. Takizawa, and T. E. Tezduyar, *Computational fluid-structure interaction: methods and applications.* John Wiley & Sons, 2013.

[4] Ansys-Campus, "Ansys fluent fluid structure interaction with ansys mechanical," 2022. [Online]. Available: https://jam8.sapjam.com/groups/mkkT44xgiV0qGZLB677BPZ/documents/OL85C6YZH06CF2sFarJO8G/slide_viewer (Accessed: 2022-02-21).

[5] "Resonance." [Online]. Available: https://www.britannica.com/science/resonance-vibration (Accessed: 2022-02-02).

[6] Z.-F. Fu and J. He, *Modal analysis.* Elsevier, 2001.

[7] P. Avitabile, *Modal testing: a practitioner's guide.* John Wiley & Sons, 2017.

[8] S. Crandall, "The role of damping in vibration theory," *Journal of Sound and Vibration*, vol. 11, no. 1, pp. 3–18, 1970. [Online]. Available: https://www.sciencedirect.com/science/article/pii/S0022460X70801055

[9] A. Jeary, "Damping in structures," *Journal of wind engineering and industrial aerodynamics*, vol. 72, pp. 345–355, 1997.

[10] G. Radoičić and M. Jovanović, "Experimental identification of overall structural damping of system," *Strojniški vestnik-Journal of Mechanical Engineering*, vol. 59, no. 4, pp. 260–268, 2013.

[11] D. J. Inman and R. C. Singh, *Engineering vibration.*, 4th ed. Pearson, 2013.

[12] R. E. Blake, "Basic vibration theory," *Shock and vibration handbook*, vol. 1, 1961.

[13] A. Wimshurst, “Large eddy simulation (LES),” A video series at https://www.youtube.com/watch?v=r5vP45_6fB4&list=PLnJ8lIgfDbkoPrNWatlYdROiPrRU4XeUA (2020).

[14] C. Pozrikidis, *Fluid dynamics - Theory, Computation and Numerical Simulation.* Springer, 2017.

[15] I. P. Castro and C. Vanderwel, *Turbulent Flows: an Introduction.* IOP Publishing, 2021. [Online]. Available: https://dx.doi.org/10.1088/978-0-7503-3619-2

[16] “Skin friction coefficient,” 2016. [Online]. Available: https://www.cfd-online.com/Wiki/Skin_friction_coefficient (Accessed: 2022-04-21).

[17] P. Hutcheson and T. Berg, “Ansys,” Private communication, 2021-2022.

[18] J. D. Anderson Jr., *Modern Compressible Flow*, 3rd ed. 1221 Avenue of the Americas, New York, NY 10020: McGraw-Hill, 2003.

[19] “Large-scale low turbulence subsonic wind tunnel,” 2018. [Online]. Available: https://www.chalmers.se/en/departments/m2/simulator-labs/labs/chalmerswindtunnels/facility/Pages/Large-Scale-Low-Turbulence-Subsonic-wind-Tunnel.aspx (Accessed: 2022-03-08).

[20] “Chalmers’ wind tunnels.” [Online]. Available: https://www.chalmers.se/SiteCollectionDocuments/Till%C3%A4mpad%20mekanik/Chalmers%27%20Wind%20tunnels.pdf

[21] V. Chernoray, Private communication, 2022.

[22] P. Ekman, *Important Factors for Accurate Scale-Resolving Simulations of Automotive Aerodynamics.* Linköping University Electronic Press, 2020, vol. 2068.

A

Appendix

A.1 Displacement of the antenna in y-direction

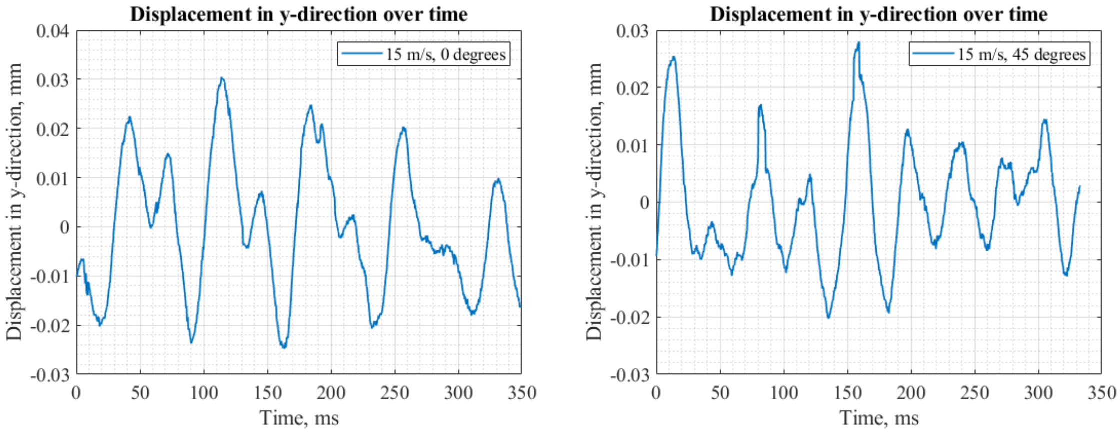

(a) 15 m/s, 0°

(b) 15 m/s, 45°

Figure A.1: Displacement of the antenna from the cases with a constant wind load of 15 m/s measured in the y-direction. The angle of the wind is: (a) 0° and (b) 45°.

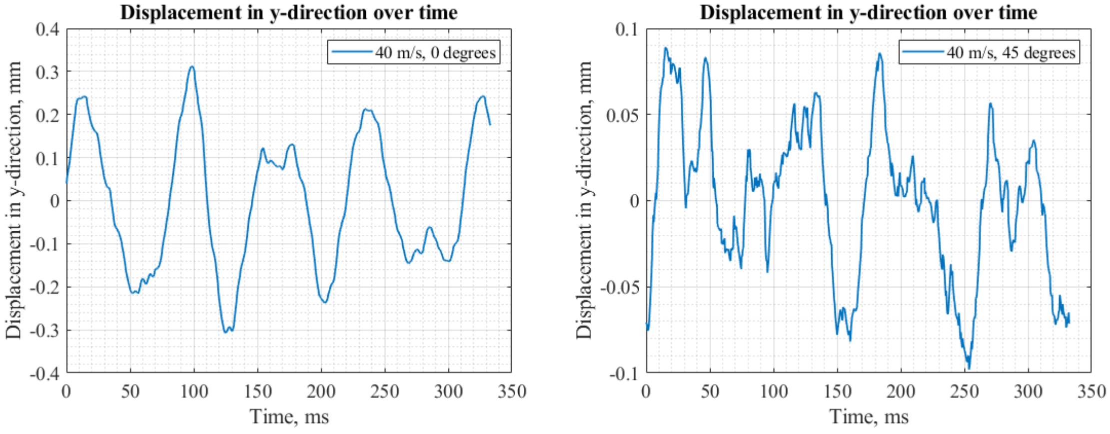

(a) *40 m/s, 0°* (b) *40 m/s, 45°*

Figure A.2: Displacement of the antenna from the cases with a constant wind load of 40 m/s measured in the y-direction. The angle of the wind is: (a) 0° and (b) 45°.

A.2 Hammer impulse tests on the antenna structure

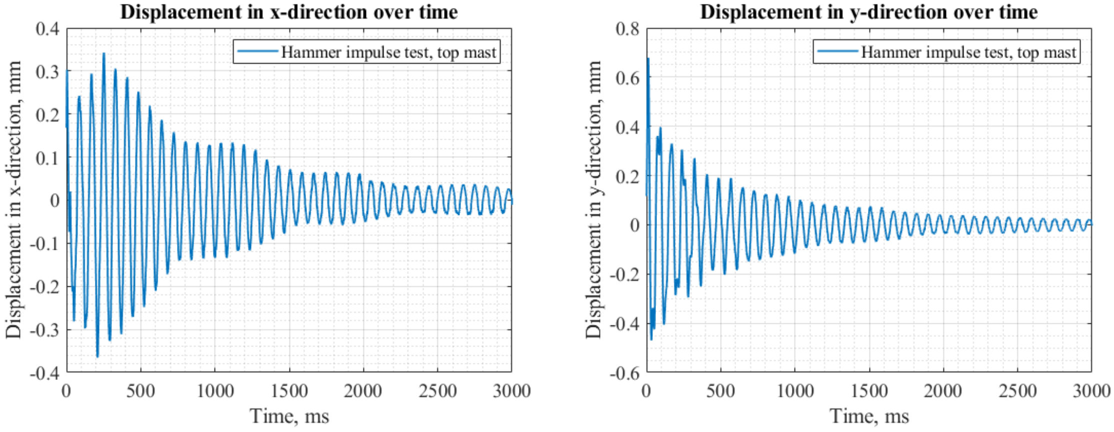

(a) *Top mast, x-direction* (b) *Top mast, y-direction*

Figure A.3: Displacement of the antenna over time for the hammer impulse test with impact location at the top mast in (a) the x-direction and (b) the y-direction.

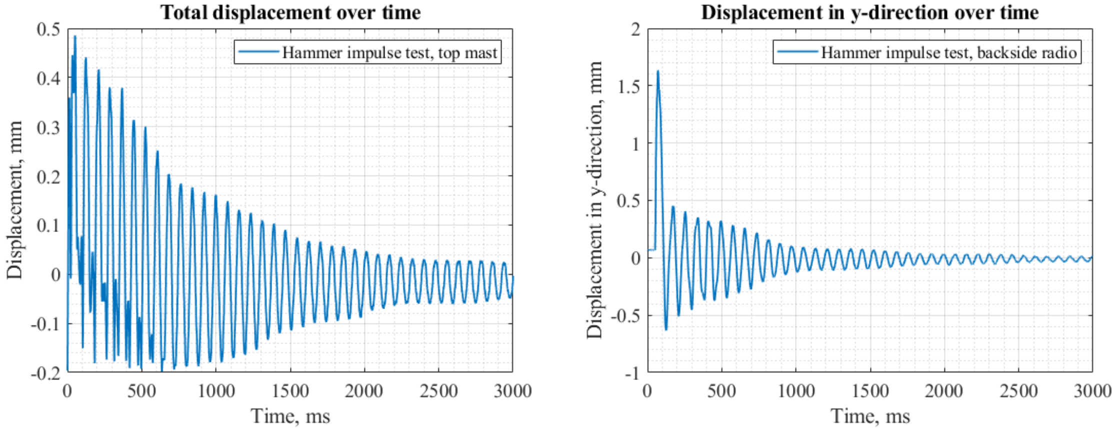

(a) Top mast, xy-direction

(b) Backside radio, y-direction

Figure A.4: Displacement of the antenna over time for the hammer impulse test with impact location at (a) the top mast in the xy-direction and (b) the backside radio in the y-direction.

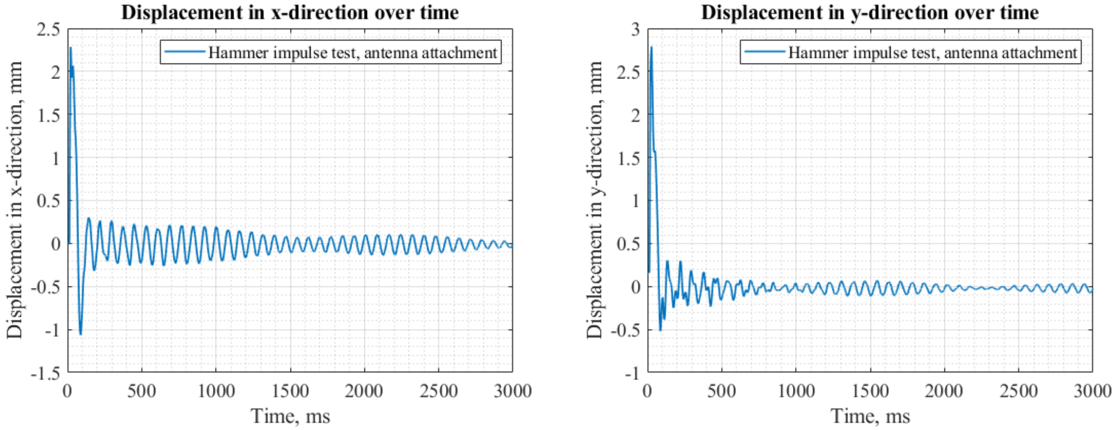

(a) Antenna attachment, x-direction

(b) Antenna attachment, y-direction

Figure A.5: Displacement of the antenna over time for the hammer impulse test with impact location at the antenna attachment in (a) the x-direction and (b) the y-direction.

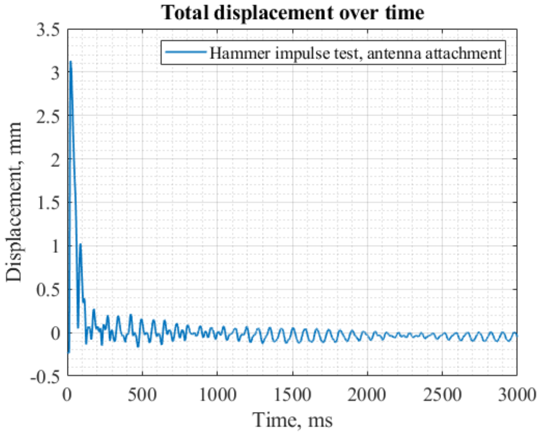

Figure A.6: Displacement of the antenna over time for the hammer impulse test with impact location at the antenna attachment in the xy-direction.

A.3 Spectral analysis plots

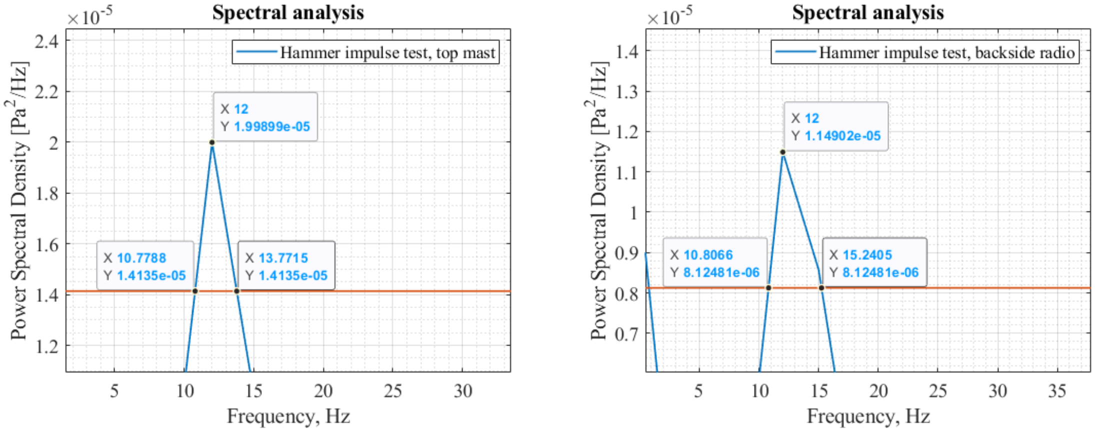

(a) Top mast *(b) Backside radio*

Figure A.7: The spectral analysis for the hammer impulse test with impact location at (a) the top mast and (b) the backside radio. The horizontal line corresponds to the $A_{max}/\sqrt{2}$ *amplitude which is used to determine the frequencies for the half-power bandwidth method.*

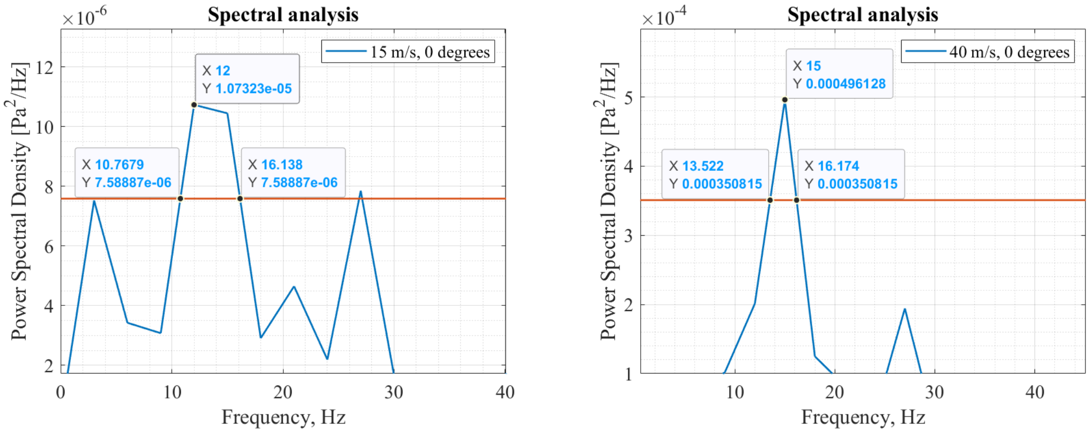

(a) 15 m/s, 0° *(b) 40 m/s, 0°*

Figure A.8: The spectral analysis for the 0° case with constant wind load of (a) 15 m/s and (b) 40 m/s. The horizontal line corresponds to the $A_{max}/\sqrt{2}$ *amplitude which is used to determine the frequencies for the half-power bandwidth method.*

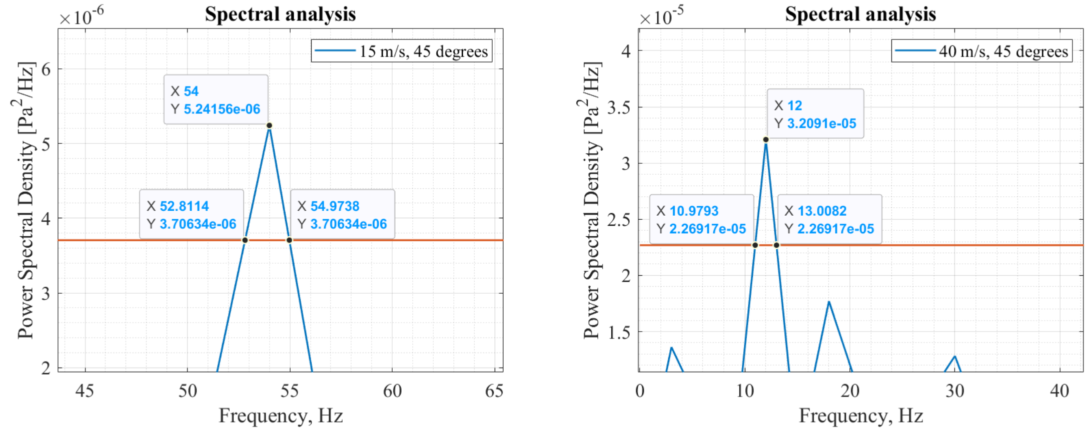

(a) 15 m/s, 45° *(b) 40 m/s, 45°*

Figure A.9: The spectral analysis for the 45° case with constant wind load of (a) 15 m/s and (b) 40 m/s. The horizontal line corresponds to the $A_{max}/\sqrt{2}$ *amplitude which is used to determine the frequencies for the half-power bandwidth method.*

A.4 Undamped displacement of the antenna

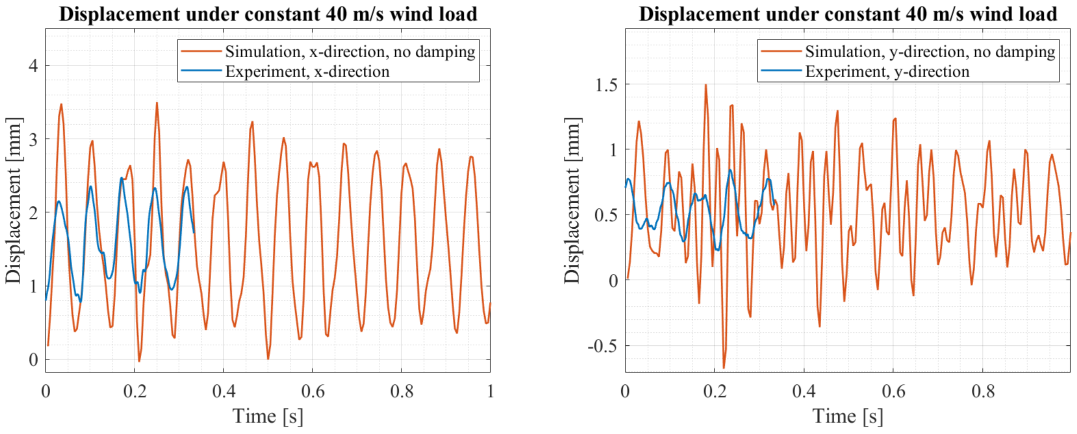

(a) Displacement in x-direction

(b) Displacement in y-direction

Figure A.10: Comparison of the displacement of the antenna in a) the x-direction and b) in the y-direction between the experiment and the undamped simulation.

A.5 Additional contour plots of the flow field

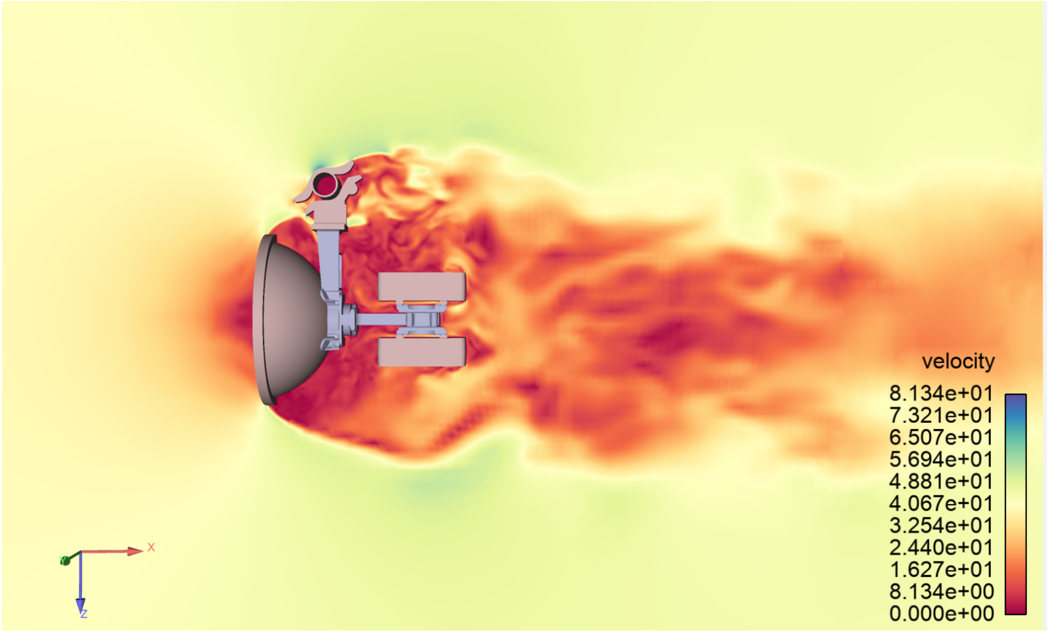

Figure A.11: The velocity field from a completed FSI Simulation. The velocity field changes with each time step.

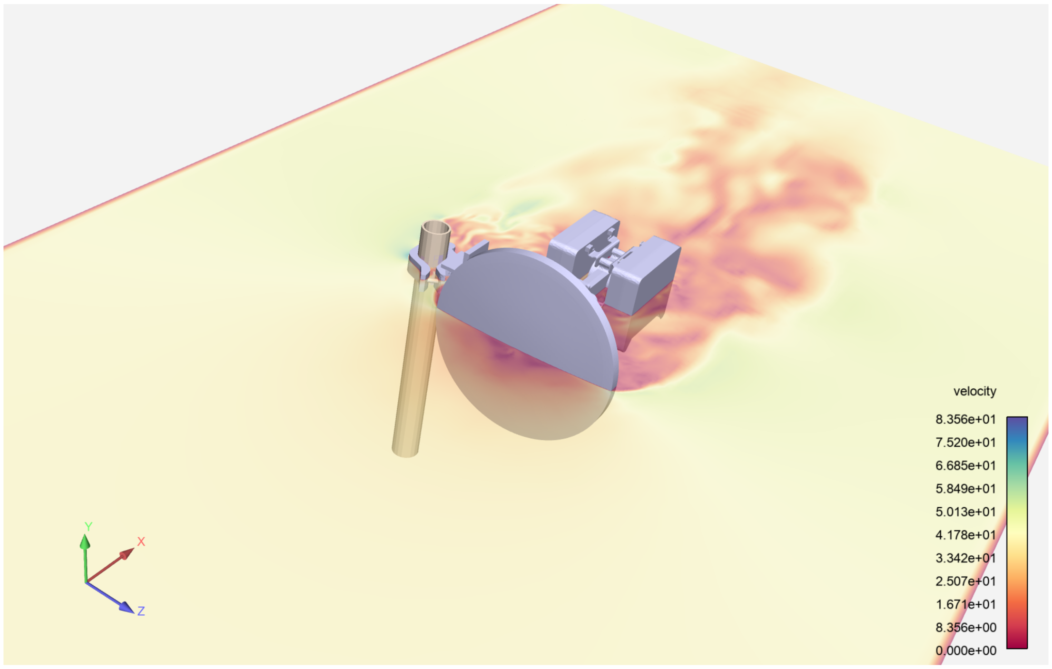

Figure A.12: The plane where Figure A.11 is shown.

DEPARTMENT OF MECHANICS AND MARITIME SCIENCES
CHALMERS UNIVERSITY OF TECHNOLOGY
Gothenburg, Sweden 2022
www.chalmers.se